

# Viscoelastic effects of immiscible liquid-liquid displacement in microchannels with bends

**Accepted Manuscript:** This article has been accepted for publication and undergone full peer review but has not been through the copyediting, typesetting, pagination, and proofreading process, which may lead to differences between this version and the Version of Record.

Cite as: Physics of Fluids (in press) (2022); <https://doi.org/10.1063/5.0091501>

Submitted: 15 March 2022 • Accepted: 30 June 2022 • Accepted Manuscript Online: 05 July 2022

 Seng Hoe Hue,  Loïc Chagot and  Panagiota Angeli



View Online



Export Citation



CrossMark

## ARTICLES YOU MAY BE INTERESTED IN

[Droplet impact dynamics over a range of capillary numbers and surface wettability: Assessment of moving contact line models and energy budget analysis](#)

Physics of Fluids **34**, 052119 (2022); <https://doi.org/10.1063/5.0087663>

[Insights into the dynamics of non-Newtonian droplet formation in a T-junction microchannel](#)

Physics of Fluids **34**, 062001 (2022); <https://doi.org/10.1063/5.0092012>

[Interface evolution characteristics of dual droplet successive oblique impact on liquid film](#)

Physics of Fluids **34**, 062115 (2022); <https://doi.org/10.1063/5.0096585>

APL Machine Learning

Open, quality research for the networking communities

**Now Open for Submissions**

LEARN MORE



Physics of Fluids (in press) (2022); <https://doi.org/10.1063/5.0091501>

(c) 2022 Author(s).

## Title: Viscoelastic effects of immiscible liquid-liquid displacement in microchannels with bends.

### Authors:

Seng Hoe Hue, Loïc Chagot, Panagiota Angeli\*

\*Corresponding author: [p.angeli@ucl.ac.uk](mailto:p.angeli@ucl.ac.uk)

### Affiliation:

ThAMeS Multiphase, Department of Chemical Engineering, University College London, Torrington Place, London, WC1E 7JE, UK

### Abstract

The displacement flow of an organic Newtonian fluid by a pure viscoelastic aqueous solution is experimentally investigated inside a circular microchannel of 200  $\mu\text{m}$ . Displacement is commonly encountered in many industrial applications, from cleaning and decontamination to enhanced oil recovery. In this study, a pure viscoelastic fluid with no shear-thinning properties (known as Boger fluid) made up of polyethylene oxide (PEO), polyethylene glycol (PEG) and zinc chloride ( $\text{ZnCl}_2$ ) is used to displace an immiscible organic liquid (silicone oil). The results were compared against those from displacement with a Newtonian fluid of similar density and viscosity as the viscoelastic one. High speed imaging is used to track both the residual film thickness of the organic phase and the interface deformations during displacement. It is found that the Boger fluid displacing phase produces a thinner displaced phase film compared to the Newtonian fluid, particularly at high capillary numbers. A correlation is proposed for the film thickness which includes the Weissenberg number for the viscoelastic case. After the displacement front, the interface becomes unstable with two modes of instability identified. In the case of the Boger fluid, the two modes of instability are core shifting, which is also present in the Newtonian case, and a periodic instability from the elastic stresses during displacement. Additionally, the shape of the interfacial instabilities switches freely from asymmetric to axisymmetric ones throughout the flow. The frequency of the periodic instabilities increases with the displacing phase flowrate. It was also found that microchannel bends downstream of the observation point affect the shape and frequency of the instabilities.

## I. INTRODUCTION

The displacement of a liquid from another liquid is very common in many industrial practices including oil and gas, pharmaceuticals and food and beverages. A common application of fluid displacement in the oil and gas industry is in enhanced oil recovery (EOR), whereby fluids are injected into end-of-life oil reservoirs to increase the recovery of crude oil that remains trapped in porous rocks. In addition, surfactant or polymer laden liquids are often used to clean or decontaminate surfaces, in both enclosed and open geometries.

When a fluid displaces a liquid, some of the initial liquid remains trapped on the wall behind the displacing front. Known as displacement inefficiency, the residual film thickness of the initial fluid trapped on the wall is larger (up to 56% of the channel diameter<sup>1</sup>) when the injected (displacing) fluid is less viscous than the initial (displaced) one. This could be a problem when displacement is used for the cleaning and decontamination of pipeline walls, as additional effort such as the use of mechanical arms or high-speed liquid jets is required to completely remove the trapped film<sup>2,3</sup>. In EOR, residual films during displacement reduce the efficiency of the process. This is often rectified by changing the properties of the displacing phase, for example, by adding surfactants or polymers<sup>4,5</sup>

There are many studies on the displacement phenomena involving Newtonian liquids in large channels<sup>6–9</sup> and more recently in small channels of internal diameter below 10 mm<sup>10–13</sup>. Small and microfluidic channels and even pillared microchannels are often used for the study of EOR phenomena as they mimic the porous rocks in oil reservoir wells<sup>14,15</sup>. During the initial displacement phenomena, the displacing phase forms a ‘finger’ front against the initially stagnant phase, leaving behind a residual film along the channel wall. Film thickness has been studied extensively for Newtonian fluid pairs with the first recorded work by Fairbrother and Stubbs<sup>16</sup> concerning an air bubble displacing an initially stagnant liquid phase. A number of correlations has been produced for the residual film thickness on the channel wall for low capillary numbers below 2, which indicated a power law dependence of the film thickness on the capillary number<sup>1,17,18</sup>. Studies at higher capillary numbers, showed additional dependence of the film thickness on the Reynolds and Weber numbers, as inertial effects become important<sup>19,20</sup>.

Behind the displacement front, perturbations due to interfacial instabilities appear, in the shape of wavy patterns along the interface of the two fluids. Interfacial instabilities occur when there is energy transfer across the interface, typically due to density or viscosity stratifications, as seen in instabilities such as Kelvin-Helmholtz (due to the higher velocity of the lower density fluid), Taylor-Rayleigh (due to the vertical movement of higher density fluid against the lower density one), Saffman-Taylor (due to the higher velocity of the lower viscosity fluid in a wide

channel) and Miles (due to the higher velocity of the lower density fluid, with a large depth of the denser fluid)<sup>21–23</sup>. The presence of density or viscosity jump across the interface causes a large change in the velocity profile; in order to maintain velocity continuity, a net work must be done by the axial flow in the tangential direction, leading to the deformation of the interface<sup>24</sup>.

In an enclosed space, these instabilities can be compared directly to the interfacial instabilities that occur in core annular flows inside channels, but with the annulus phase having zero flowrate. Charru and Hinch<sup>25</sup> suggested that the interfacial instabilities are further strengthened when small perturbations, advected by the flow, produce vortices which are out of phase with the interface height in both phases. This effect is more significant at the displacing core compared to the residual film, as the core layer is thicker relative to the film, while the fluid is less viscous. The difference in the sizes of vortices on the two sides of the interface causes changes in the flow fields of both liquids in the channel. Locally, if the core vortices are larger than those in the film, the interface moves outward, observed as crests which, when moved by the flow, resemble travelling instability waves.

Flows with stratified layers of fluids with different viscosities are often unstable when the core is less viscous than the film/annulus, apart from a small range known as perfectly core annular flow (PCAF). Achieving PCAF experimentally can be very difficult due to physical restrictions such as channel size, core diameter and flowrates of both phases, as discussed in a series of experimental and analytical works by Joseph and co-workers<sup>9,26–29</sup>. When the flow is unstable, any small perturbations at the channel entrance would result in an instability downstream as the growth rate of the instability is positive<sup>30–32</sup>. The experimental results have also been compared with predictions from stability analysis with good agreement<sup>26,27,33</sup>. Foroughi et al.<sup>11</sup> measured the change in the diameter of the water core as well as the length of the waves formed and compared them with results of both linear and non-linear stability analysis, with the former having better agreement with the experimental data at low Weber numbers while the latter had an overall better fit at all flowrates.

Most studies also showed that the displacement front was initially stable with a flat interface between the two phases, with the finger located at the center of the channel. With the onset of interfacial instability, when the core remains intact, symmetrical interfacial waves (similar to the pinching of the core fluid) were seen at first, followed by asymmetrical waves (sinusoidal travelling waves). On the contrary, if the core breaks up, plug, slug and dispersed flows are observed<sup>9,28</sup>. With aqueous displacing phase, the displacing core was also observed to shift from the center to one side of the channel<sup>11,13</sup>.

In contrast, the literature available on displacement and instabilities with non-Newtonian fluids is limited. Of the studies available, many have considered displacement of shear-thinning or

yield-stress fluids<sup>34–37</sup>. Displacement involving two miscible complex liquids<sup>38,39</sup> as well as displacement of a viscoelastic fluid by a Newtonian one<sup>40–43</sup> have also been investigated. The latter is interesting for the drilling of oil wells, as water is often used to displace the viscoelastic drilling muds. For the displacement in a microchannel of a Newtonian liquid by a viscoelastic one however, there is only a short experimental study by Soares et. al<sup>44</sup> on the displacement efficiency. This is despite the common use of viscoelastic fluids for cleaning and in tertiary EOR, where a combination of polymers and surfactants are commonly used. The displacement of viscoelastic fluids in pillared microchannels<sup>14</sup> and Hele-Shaw configurations<sup>5,34,43,45,46</sup> indicated an increase in the maximum finger growth rate and the wavelength of the largest interfacial instability, when compared to the Newtonian case. Saintyves et al.<sup>43</sup>, from experimental studies in a Hele-Shaw cell, suggested that the elasticity of a viscoelastic fluid in the displaced phase causes an increase in the internal mixing due to an additional elastic stress, which increases the interfacial instabilities. Gan et al.<sup>47</sup>, from experiments in converging-diverging geometries, also discussed that instabilities at the interface between two viscoelastic fluids will increase internal mixing over short mixing lengths. Hence, overall displacement efficiency is better, with larger percentage of the displaced phase recovered.

In this work, we study the displacement of an initially stagnant organic phase by a pure viscoelastic (Boger) fluid in a straight microchannel with downstream U-bends. To the best of our knowledge, this is the first time a complete study of the immiscible displacement phenomena is carried out in a microchannel involving a displacing Boger fluid. Using a small internal diameter channel, only a single displacement front is observed, which facilitated the study of the effects of varying flowrates and displacing fluid properties. This is in contrast to studies in Hele-Shaw cells or in infinite width microchannels whereby multiple finger fronts are usually seen. In addition, the Boger fluid contains an ionic salt in the polymeric solution, which better mimics the conditions in an actual EOR system, where seawater is commonly used instead of desalinated or deionized water. In what follows, the rheological properties of the viscoelastic phase are characterized and the experimental procedures for the displacement are described. From the results, a residual film thickness correlation is proposed for the Boger-Newtonian fluid displacement for the first time, taking into account the elastic effects of the displacing phase. The interfacial instabilities that develop behind the displacement front are then investigated and the modes of instability are identified and compared for the Newtonian-Newtonian and the Boger-Newtonian cases. The effects on the instabilities of bends in the microchannel are finally discussed.

## II. Experimental Methodology

### A. Fluid pairs

The test fluids selected for the displacement experiments need to satisfy a number of criteria. The two phases should be immiscible, non-reactive, and their viscosities should be high enough to minimise inertial effects, while keeping the frictional pressure drop inside the microchannel within the limits of the pressure that the syringe pumps can deliver. In the experiments, the displacing phase will be less viscous than the displaced phase. This ensures the instabilities formed during displacement are large enough to be visible<sup>22</sup>. The refractive indexes of the two liquids are matched closely to reduce reflections along the interface during imaging. Lastly, the displaced phase should be as transparent as possible, for better imaging with the backlight used.

Silicone oil was chosen as the displaced phase, which was initially stagnant inside the channel. It was possible to maintain the viscosity and density ratios of the two liquids by blending silicon oils with different viscosities. For the Newtonian-Newtonian displacement experiments, the organic phase was prepared by gently mixing 90 wt% of 20 cSt silicone oil (VWR Chemicals) and 10 wt% of 100 cSt silicone oil (VWR Chemicals), giving a viscosity of 23.86 mPa s. Meanwhile, the aqueous phase was a solution of 10 wt% zinc chloride ( $\text{ZnCl}_2$ )(Sigma Aldrich Science) and 20 wt% of 5000 molecular weight polyethylene glycol (PEG 5000)(Sigma Aldrich Science) in deionized water, with a viscosity equal to 19.68 mPa s. Nigrosin dye (Sigma Aldrich) was then added in minute amount (1 drop per 20 ml) to help distinguish between the two phases during imaging.  $\text{ZnCl}_2$  was added to increase the refractive index of the solution, closely matching that of the organic phase and of the microchannel wall. It also makes the solution ionic, better resembling the seawater often used in EOR due to its abundance offshore. The low molecular weight PEG 5000 was added to increase the overall viscosity of the fluid. At low concentrations (<30 wt%) of PEG 5000, the aqueous solution remains Newtonian as the polymer chains are short and do not interact with one another<sup>48</sup>.

For the case of the Boger-Newtonian fluid pair, the ratio of 20 cSt to 100 cSt silicone oil for the organic phase was changed to 73.5 wt% and 26.5 wt% respectively, which produces a displaced phase with a viscosity of 32.52 mPa s, but with the same density and refractive index as the previous organic solution. According to Boger<sup>49</sup>, there are two main methods to produce a pure viscoelastic fluid with no secondary fluid characteristics, a high viscosity solvent or high molecular weight solutes. A high viscosity solvent is not possible here, as the pressure drop inside the microchannel will become too large and the latter approach is used instead. The Boger fluid was prepared by adding 0.05 wt% (500 ppm) of 5,000,000 molecular weight polyethylene oxide (PEO 5M) (Sigma Aldrich Science) to the already prepared aqueous

Newtonian solution described above. The short polymeric chains of PEG 5000 are located in between the longer chains of PEO 5M, thus preventing them from sliding past each other during shear. This combination of the PEG 5000 and PEO 5M prevents any shear-thinning effects often seen in other polymeric solutions and have been used to some success previously<sup>38,48</sup>.

For the rheological measurements, a rheometer (MCR302, Anton Paar) with a cone and plate geometry (50 mm, 1° angle) was used. The rheometer was equipped with a Peltier plate and the operating temperature was set to 25°C to match the temperature of the displacement experiments. The densities of all three liquids were obtained with the density bottle measurement technique. Interfacial tensions between the organic and aqueous phases were measured using a force tensiometer (K100c, KRÜSS GmbH), with the Wilhelmy plate attachment, while the refractive indexes were measured using an Abbe refractometer (Edmund Optics). All measurements were conducted at 25°C. A summary of the properties of all fluid pairs is given in Table I:

**Table I.** Physical properties of fluid pairs.

Fluid Pair	Fluid Phase	Density (kg/m <sup>3</sup> )	Density Ratio $\left(l = \frac{\rho_{aq}}{\rho_o}\right)$	Viscosity (mPa s)	Viscosity Ratio $\left(m = \frac{\mu_{aq}}{\mu_o}\right)$	Interfacial Tension (mN/m)	Refractive Index
Newtonian-Newtonian	Organic	950	1.146	23.858	0.824	25.79	1.40
	Aqueous	1089		19.677			1.39
Boger-Newtonian	Organic	950	1.146	32.520	0.821	26.08	1.40
	Aqueous	1090		26.685			1.39

### B. Rheological Measurements

Shear rate-shear stress measurements were performed for all solutions to obtain the viscosity data shown in Table I. It was found that the viscosities are constant for both the Newtonian and the Boger fluids, for shear rates between 1 and 400 s<sup>-1</sup>, with the Boger fluid having less than 5% variations throughout (inset Fig. 1). This range is larger than the range of shear rates experienced in the microchannel during displacement.

The degree of viscoelasticity of a fluid is typically linked to the first normal stress difference. However, the viscosity of the Boger solution chosen is low and the first normal stress difference could not be measured accurately, as it was below the sensitivity of the rheometer. Instead, the relaxation time of the fluid was obtained from small amplitude oscillatory shear (SAOS) tests in the linear viscoelastic region (LVER). For a shear strain amplitude of 1%

(below the critical LVER value of 2%), the oscillation frequencies were varied across three decades, between 0.1 and 100 rad/s, and the resulting  $G'$  and  $G''$  were measured (Fig. 1). The intersection of the two moduli at around 100 rad/s, gives a relaxation time of approximately 0.063 s.

The measured moduli were also fitted with a generalised Maxwell multi-model and a good fit was obtained when two components of the relaxation time were considered, at 0.07 and 0.004 s. The former is comparable to the relaxation time found from the interception of the storage and loss moduli in Fig. 1.

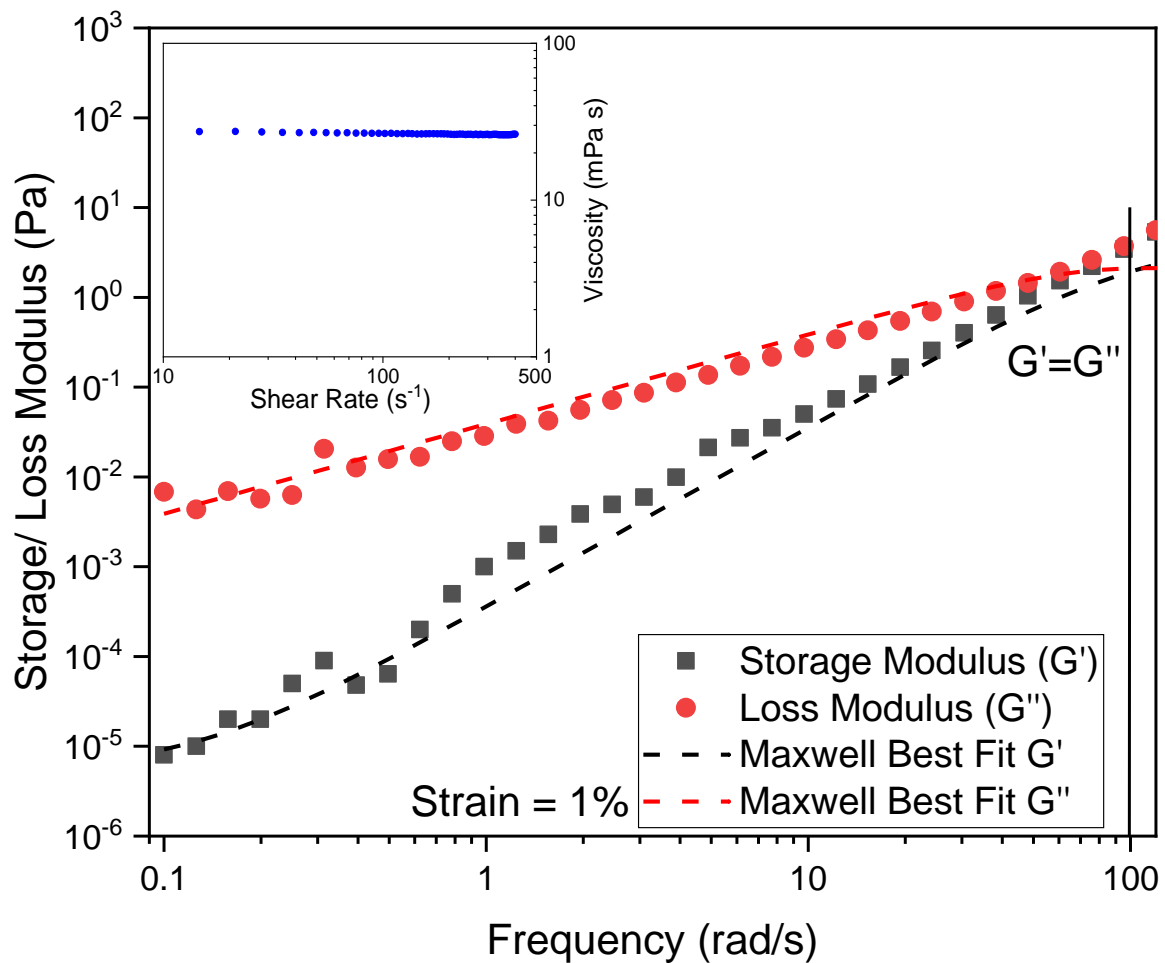


**Fig. 1.** SAOS tests for the Boger fluid at 1% strain to obtain the storage and loss moduli. Dotted lines are the Maxwell model with two components of relaxation time. Inset: viscosity curve for the Boger fluid.

**Table II.** Relaxation times of Boger fluid, calculated from rheological data and two component Maxwell model fitting.

Techniques	Relaxation times (s)
Rheometer measurements ( $G'$ and $G''$ intersection point)	0.063
Generalised Maxwell Model	0.0733



(Two component multi-model)	0.0048
-----------------------------	--------

### C. Displacement Experimental Setup

To study the displacement phenomena, a high-speed camera (Phantom V1212, Vision Research, Ametek) was used with a 50 $\times$  microscopic lens attachment (Mitutoyo Ltd.), giving a depth of field of 0.9  $\mu\text{m}$ . The exposure was set to a constant value of 10  $\mu\text{s}$  and the camera was operated at 5000 fps. Illumination was provided by a continuous white LED bright light (GS Vitec), located opposite the camera (Fig. 2(i)). Experiments were carried out in a hydrophobic coated circular glass microchannel (Dolomite) of 200  $\mu\text{m}$  internal diameter. This enabled the observation of displacement in a straight section, followed by bends downstream (Fig. 2(ii)). The length of the straight section of the microchannel between the inlet and the first bend is 34mm, with the imaging carried out at 50 diameters (10 mm) from the channel inlet. Fig. 2(ii) also shows the position of the inlet and the imaging window of the microchannel.

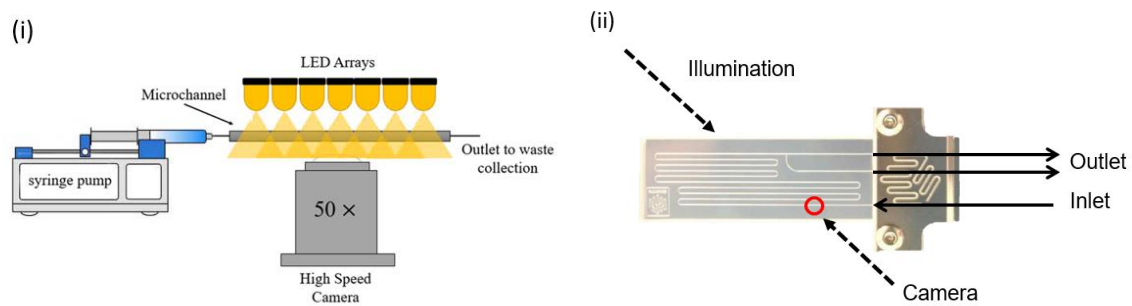


**Fig. 2.** (i) Schematic of the displacement experimental setup. (ii) Detailed microchannel configurations with inlet and outlet line opposite to the conventional direction, measurement window (marked in red circle) and the location of the bends downstream. The camera and LED are parallel to the microchannel, on opposite sides.

Using a high precision syringe pump (KD Scientific), the flowrate of the displacing phase was varied between 0.03 ml/min to 0.35 ml/min, at intervals of 0.02 ml/min at the lower flowrates (between 0.03 and 0.1 ml/min), and 0.05 ml/min at the higher ones (between 0.1 and 0.35 ml/min), totaling 10 different flowrates for the film thickness measurements. For the interfacial instability measurements, flowrates were varied between 0.05 and 0.2 ml/min.

From velocity profile measurements using particle shadowgraphy in single phase flow of a water-glycerin solution with the same viscosity as the test fluid, between 19.67 and 32.52 mPa s, it was found that the syringe pump had fluctuations between 2 - 5 % of the mean flowrate value, which are within the measured accuracy during the displacement experiments. The fluctuations would act as the source of perturbations initiating the instabilities of the interface after the initial displacement.

#### D. Image Post Processing Methodology

The captured images of the instabilities were processed with Matlab 2020a (Mathworks) in several stages, summarized graphically in Fig. 3. Due to the slight refractive index mismatch between the channel wall, displaced and displacing phases, the interface and the channel walls appear as thick lines, which after processing, produce two lines as seen in Fig. 3(ii). The difference between the two lines is below 1 % of the channel diameter, which is within the acceptable error, discussed below. However, to ensure consistency in the film thickness measurements, the outer lines are taken for both the interface and the wall.

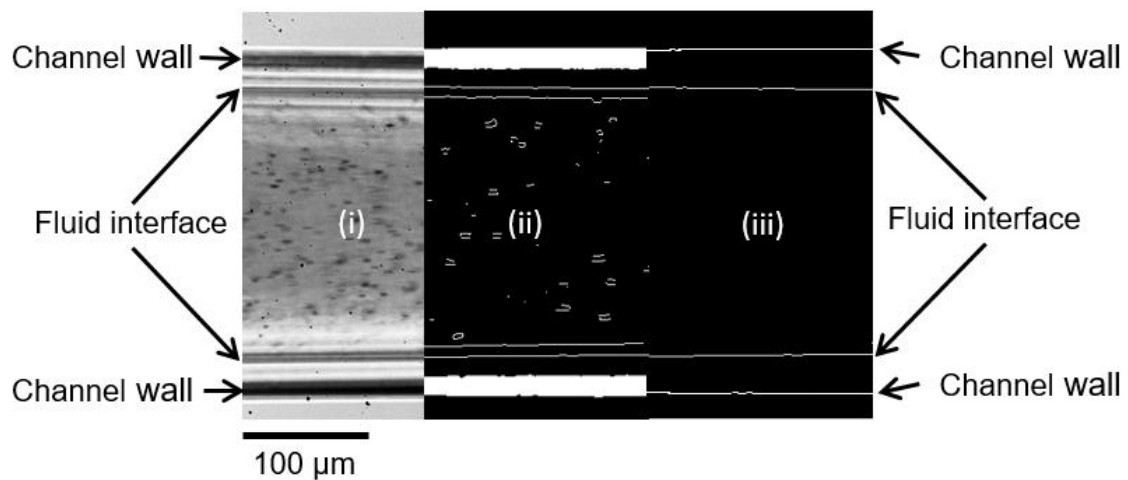


**Fig. 3.** Summary of post-processing steps to obtain the residual film thickness: (i) unprocessed image (ii) image binarization and interface detection (iii) removal of noise and shadows. Images are from the Newtonian-Newtonian displacement for a flowrate of 0.1 ml/min.

The fluid interface is tracked at a particular location in the image for 5 s after the onset of the first instability. The interface position is averaged over 5 consecutive pixels to reduce noise. Additionally, outlier data points, which are 5 standard deviations away from the interfacial position of the neighbouring frame, are removed and replaced with linear interpolated points

The smallest error in the residual film thickness measurements is 2 pixels, accounting for errors in the measurement of the channel wall and of the liquid interface; with an image resolution of  $768 \times 576$  pixels, this equals to  $5 \mu\text{m}$  or 2.5 % of channel diameter. For the interface tracking, the smallest error is 1 pixel, or  $2 \mu\text{m}$  (1.25 %) for an image resolution of  $768 \times 400$  pixels.

### III. Results

#### A. Initial displacement front and residual film thickness

At first contact between the two phases in the microchannel, the displacing aqueous phase forms a ‘finger’ front, leaving a residual film of the initial organic phase on the channel wall, as illustrated in Fig. 4. If the thickness of the remaining film is large, this means that a significant amount of the initial liquid remains trapped on the channel wall and the displacement process is not very efficient. The thicker the film is, the more of the initial liquid remains trapped on the channel wall, decreasing the efficiency of the displacement process. The film thickness is the same for the top and the bottom part of the channel initially as the Bond number ( $Bo = \Delta\rho g D^2 / \sigma$ , where  $\Delta\rho$  is the density difference between the two phases,  $g$  is the gravitational acceleration,  $D$  is the channel diameter and  $\sigma$  is the interfacial tension of the two phases) is small and the density difference between the phases does not affect the position of the displacement front. Measurements of the film thickness were taken at positions right after the finger front, which is when the interface between the two phases is flat<sup>50</sup>. For all cases studied, the residual film thickness increases with flowrate, as expected from previous literature<sup>1,16–20,51</sup>. When the flow of the displacing phase is stopped, the core thickness decreases over time, with the displaced phase squeezing the core, forming plugs eventually. This is attributed to the dominance of surface tension forces when flow is stopped.

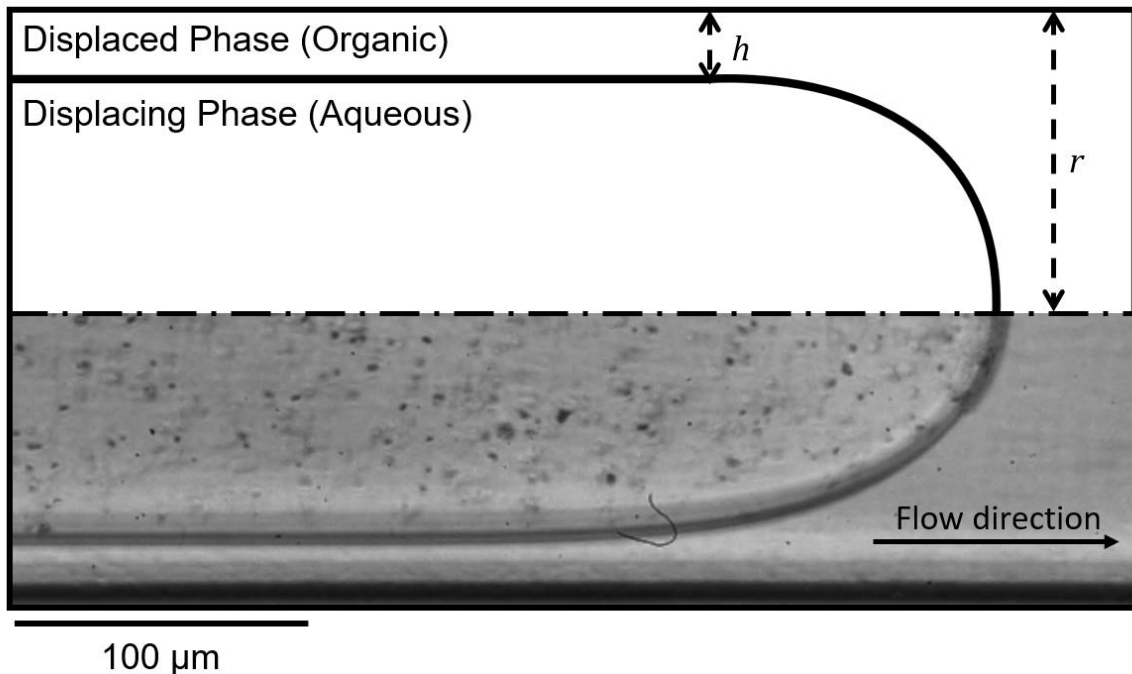


**Fig. 4.** Schematics (top half) and comparison with experimental image (bottom half) of a displacement front.

## 1) Newtonian-Newtonian pair

For the Newtonian-Newtonian displacement case, the residual film thickness,  $h$ , non-dimensionalised with the channel radius,  $r$ , is shown against the capillary number ( $Ca = \mu_{aq}V_f/\sigma$ , where  $\mu_{aq}$  is the viscosity of the displacing phase and  $V_f$  is the finger front velocity) in Fig. 5. In this study, the capillary number is based on the displacing phase to allow better comparison with previous literature.

It has been shown previously in experimental<sup>50,52</sup> and numerical studies<sup>10</sup>, that the viscosity ratio,  $m$ , of the displacing over the displaced phase can affect the film thickness. This is in contrast to gas-liquid flows. The difference in the film thickness due to viscosity ratio can range from 30% for high capillary number flows to 10% at low  $Ca$ . Based on the Bretherton's theory for Taylor bubbles<sup>18</sup> and the work of Aussillous and Qu  r  <sup>19</sup>, Balestra et. al<sup>50</sup> developed an empirical model to predict the film thickness for viscous elongated drops in axisymmetric microchannels, which takes into account the viscosity ratio and is given by:

$$\frac{h}{r} = \frac{P(m) (3Ca^{2/3})}{1 + P(m) Q(m)(3Ca^{2/3})} \quad 10^{-3} \leq Ca \leq 1, \quad (1)$$

where  $P(m)$  and  $Q(m)$  are coefficients defined by Balestra et. al<sup>50</sup>. For a viscosity ratio of  $m = 0.8$ , the values of  $P(m)$  and  $Q(m)$  are calculated to be 0.65 and 1.8 respectively.

By comparing Eq. 1 with our experimental data (Fig. 5), a very good agreement is found with a standard error of 0.001.

## 2) Boger-Newtonian pair

The dimensionless film thickness for the aqueous Boger fluid displacing a Newtonian organic phase for the same flow rates as the Newtonian-Newtonian case is shown in Fig. 5. To the best of our knowledge, there are no correlations on the film thickness during displacement with pure viscoelastic fluids. Here, we propose the following Eq. 2 for the Boger-Newtonian fluid pair displacement by including in Eq. 1, the Weissenberg number ( $Wi = \lambda/\tau$ , where  $\lambda$  is the fluid relaxation time and  $\tau$  is the flow characteristic time; in the case of fluid displacement, the  $\tau$  can be calculated as  $\tau = D/V_f$ ).

$$\frac{h}{r} = \frac{P(m) (3Ca^{2/3})}{1 + P(m)Q(m)(3Ca^{2/3}) + K Wi^{3/2}} \quad Ca \leq 0.14, \quad (2)$$

where the fitting coefficient  $K = 1.2 \times 10^{-3}$ . In this empirical correlation,  $Wi$  is added in the denominator to include the effect of elasticity on film thickness, as the elasticity of the displacing fluid acts as an extra force to the flow<sup>20,50,52</sup>. Reynolds number ( $Re = \rho_{aq}V_fD/\mu_{aq}$ , where  $\rho_{aq}$  is the density of the displacing phase) is not considered here as the flow is at a low

velocity. Eq. 2, when plotted in Fig. 5, showed good agreement with experimental data, with a standard error of fitting of 0.001.

In our data, the change in Weissenberg and capillary numbers are directly related to the change in the velocity of the displacing phase alone, as it is hard to obtain another low viscosity Boger fluid that could flow inside a microchannel of this size. Although the value of the coefficient associated with the Weissenberg number in Eq. 2 is small, the elastic effect on the film thickness is non-negligible; at high flowrates, the residual film thickness of the organic phase when displaced by the Boger fluid is up to 7% smaller than that of the Newtonian fluid. In the Boger fluid case, an additional force, the elastic stress, is present which acts radially during displacement, increasing the thickness of the core of the displacing phase and resulting in the reduction of the residual film. The results are also in qualitative agreement with the previous displacement studies by Soares et al.<sup>44</sup> for the displacement of a similar Boger fluid in oil.

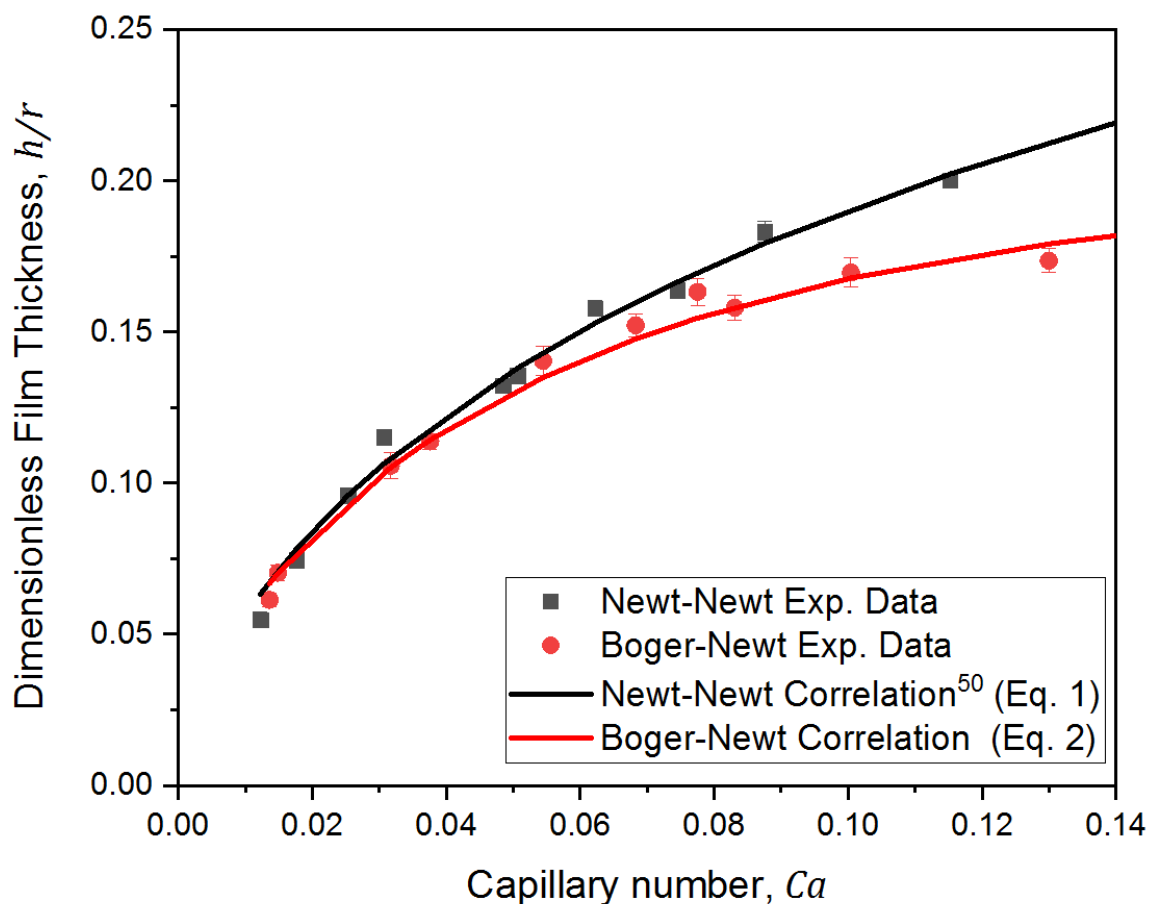


**Fig. 5.** Experimental points for film thickness against capillary number for the Newtonian-Newtonian displacement (black dots) and Boger-Newtonian displacement (red dots) and comparison with Eq. 1 and Eq. 2. Error bars indicate largest measured error as standard deviation from the average measured value.

### B. Displacement evolution, interfacial instabilities and stability analysis

Behind the initial displacement front, the residual film thickness decreases continuously until eventually the entire channel is filled with the displacing fluid. Within this time, a wave-like instability develops at the interface. The onset of the instabilities behind the displacing front depended on the flowrate as well as on the physical properties of the displacing fluid. Instabilities are developed from small initial perturbations, from fluctuations induced by the experimental setup such as inlet pumps, growing over time due to the non-negative growth rate<sup>9</sup>. The interfacial instability observed here is only due to viscosity difference between the two phases as the density difference can be safely neglected when the Bond number is lower than the critical value ( $Bo = 0.0021$ ). Even though interfacial instabilities have been studied previously, there are no detailed studies of the amplitudes and frequencies of the waves. Knowledge of the characteristic frequencies can lead to a better understanding of the instabilities, and help their experimental studies, for example by using techniques such as particle image velocimetry to obtain velocity fields.

A linear stability analysis showed that for the Newtonian-Newtonian fluid pair used here the flow is unstable. The analysis followed a similar approach to that by Foroughi et al.<sup>11</sup> as well as Funada and Joseph<sup>53</sup> and is shown in Appendix A. The dimensionless instability growth rate against the dimensionless wave number is plotted in Fig. 6, for three indicative film thicknesses, between 30  $\mu\text{m}$  and 10  $\mu\text{m}$ , representing all ranges of experimental observations. The dimensionless growth rate is defined as the rate of the change of the unstable interfacial wave amplitude while the dimensionless wave number is based on the minimum instability wavelength, normalised with the channel diameter.

The instability wavelength can be obtained by calculating the distance between two successive interfacial wave troughs. In the flowrates used here (represented in Fig. 6 by the shaded region), the flow is always unstable as the growth rate remains positive. As can be seen, an increase in the film thickness, which is associated with increased flowrates, results in an increase in the growth rate of the instability. Also, the growth rate increases with the dimensionless wave number up to a maximum value, followed by a decrease. For a fixed viscosity and density ratio between the fluids, the instability was dependent on the flowrates alone.

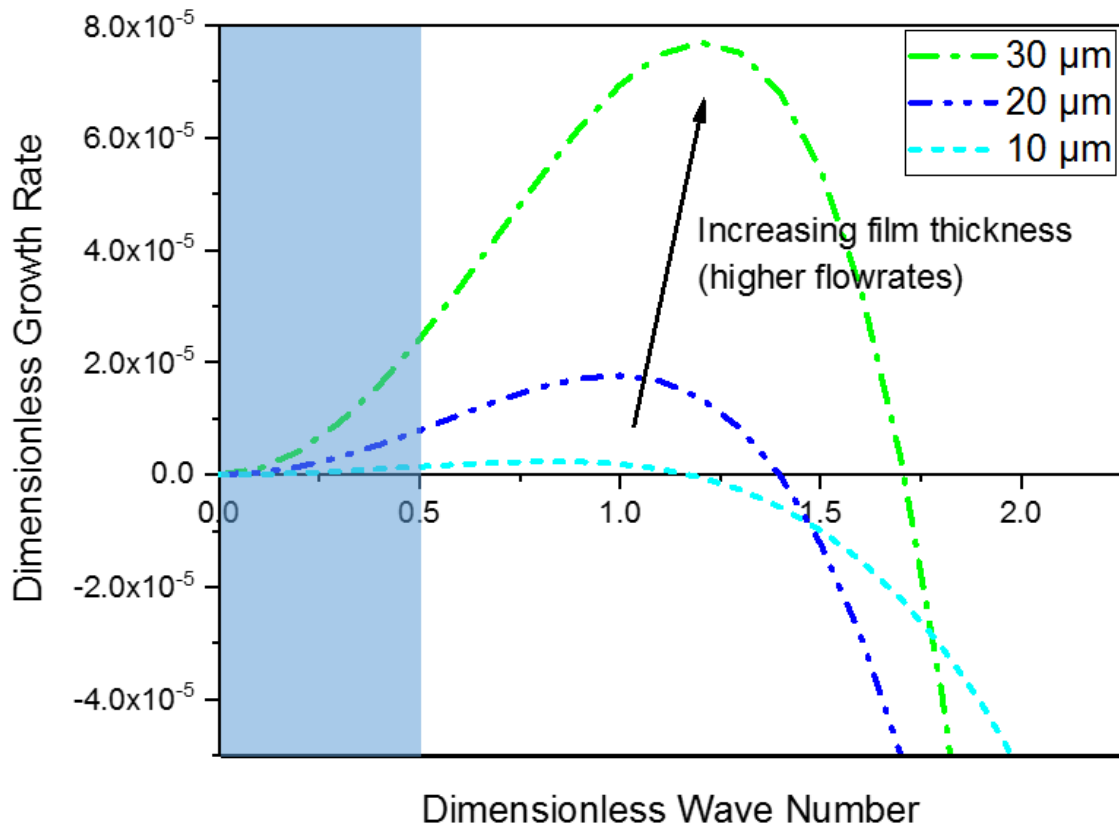


**Fig. 6.** Dimensionless interfacial instability growth rate against dimensionless wave number for increasing average film thickness. Stability analysis was done for a Newtonian-Newtonian displacement with displacing flowrate of 0.1 ml/min,  $l = 1.146$  and  $m = 0.824$ .

The first instabilities that were observed experimentally in this study are in the form of asymmetric waves. In previous studies, axisymmetric waves were first seen which transition to asymmetric ones<sup>11,13</sup>. However, the amplitudes of the initial instability waves are too small to be measured and when the first instabilities were observed, they were already asymmetric.

The time for the first observable interfacial instability to develop behind the finger front is shown in Fig. 7. This is important since the interfacial waves enhance the removal of the wall film. The time decreases exponentially with increasing flowrates for both the Newtonian-Newtonian and the Boger-Newtonian fluid cases. This is in agreement with the stability analysis calculated earlier, whereby larger displacing flowrates produce larger instability growth rates, and the first observable instabilities are seen earlier after the displacement front. For the Newtonian-Newtonian fluid pair, the time is longer than that of the Boger-Newtonian one, and the difference is as high as 50% at low flowrates, despite the similar film thickness between the two cases. At high flowrates however, the time for the onset of the instabilities is similar between the Newtonian-Newtonian and Boger-Newtonian cases. For the Boger-Newtonian displacement case, an additional force, the elastic stress is present. This augments

the interfacial instability caused by the viscosity stratification seen in the Newtonian-Newtonian case, causing the instability to be observed much earlier at low displacing phase flowrates. At high flowrates, the interfacial instabilities are detected just after the initial displacement front in both cases, at around 0.1 seconds. While the thinner film in the Boger-Newtonian case would mean lower instability growth rates (see Fig. 6) compared to the Newtonian-Newtonian one, the additional elastic stresses increase the growth rate, and as a result the time to the first observable instabilities is similar between the two cases. No stability analysis on Boger fluids has been conducted before to confirm this however.

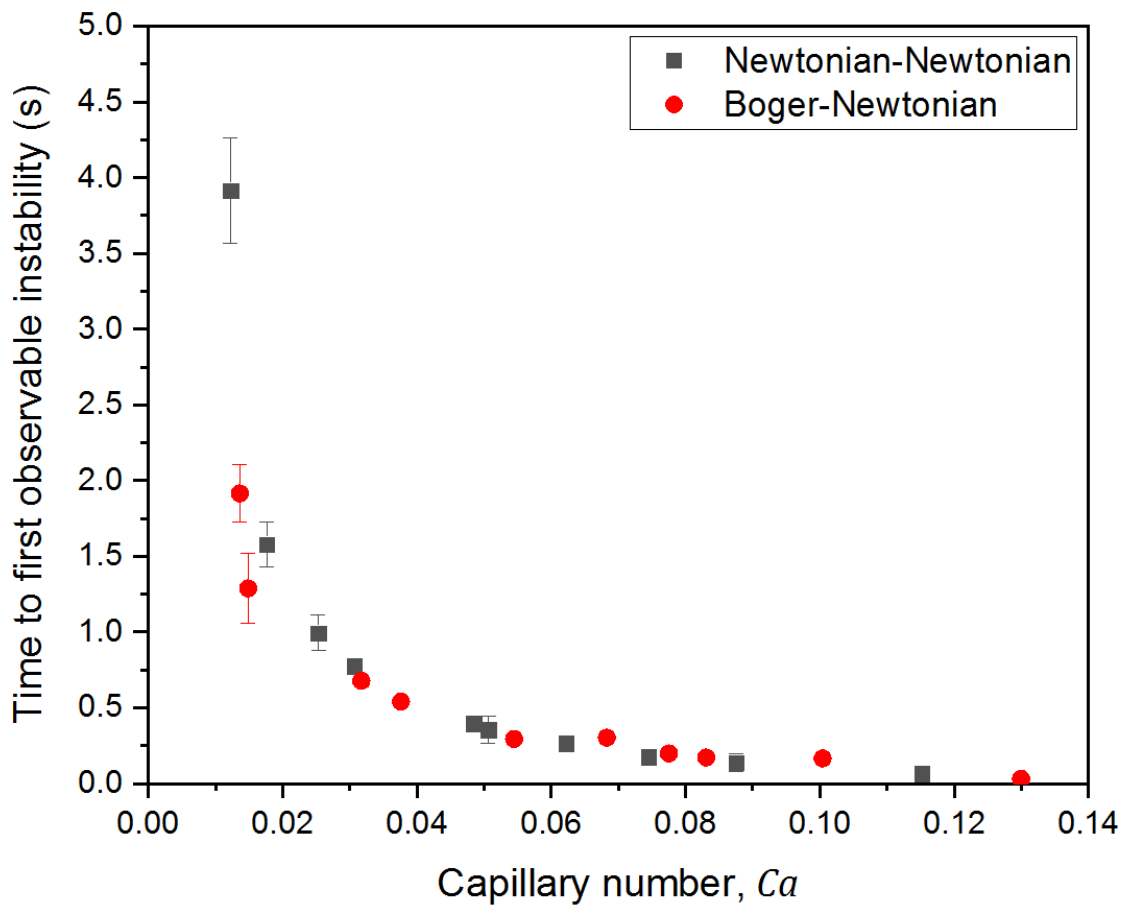


**Fig. 7.** Time for the onset of the first instability after the initial displacement front for the Newtonian-Newtonian and Boger-Newtonian fluid pairs. Error bars show the largest variation between repeated measurements.

Although large instabilities are observed, no core break up was seen. The instabilities after the onset of the first one acquired two distinctive patterns: asymmetric (Fig. 8(i)) and axisymmetric (Fig. 8(ii)) waves. The description of the instability patterns here is based on the two-dimensional images captured. However, as the circular microchannel is three dimensional, the asymmetric instabilities could have the form of corkscrew waves, while the axisymmetric instabilities could be in the form of bamboo waves, as observed previously by Chen et al.<sup>28</sup> and Bai et al.<sup>9</sup>. Due to the configuration of the microchannel on a flat substrate,



we were not able to capture the instabilities at other angles and cannot verify the actual three-dimensional shapes of the instabilities.

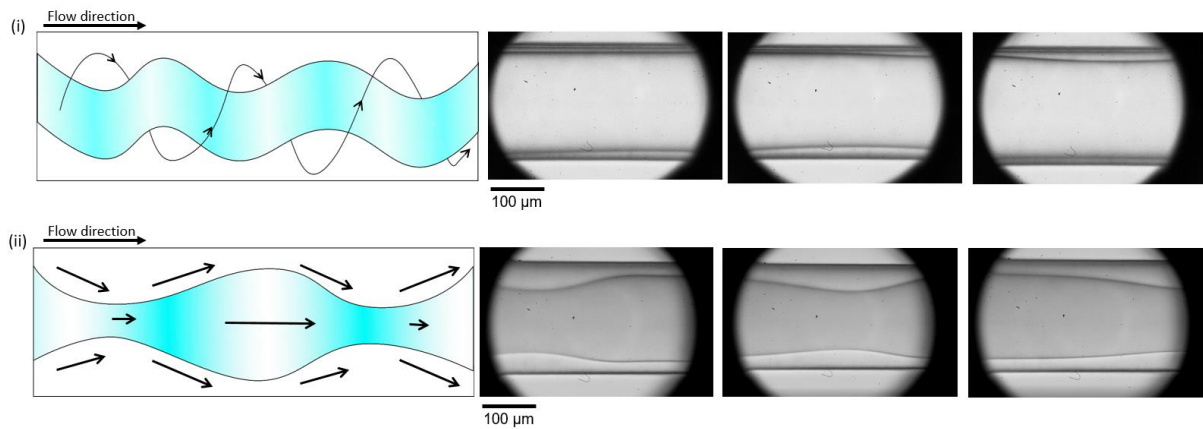


**Fig. 8.** Schematics of (i) corkscrew and (ii) bamboo waves alongside image sequences of asymmetric and axisymmetric waves captured in this study. Arrows represent the three-dimensional movement of the fluid. Images are from the Newtonian-Newtonian fluid pair displacement at 0.1 ml/min.

In this study, the instabilities could switch from one pattern to the other. When the initial waves are sheared at different rates along different parts of the interface due to the perturbations introduced at the entrance, the position of the wave crests and troughs starts to vary between the top and the bottom interface. In addition, the displacing core also shifts from the center after some time, in agreement with previous studies<sup>11,54,55</sup>, which further changes the speed of the waves. We hypothesized that this is the main reason that the instability pattern switches freely from axisymmetric to asymmetric and vice versa over the entire time of measurement; wave patterns at the top and bottom are seen to change from in-phase to out-of-phase constantly. At exactly one period apart, the top and bottom interfaces match, yielding axisymmetric waves. Likewise, when the top and bottom interfaces are out of phase, the instability is asymmetric.

### C. Interfacial instabilities for Newtonian-Newtonian displacement

Fig. 9(i) illustrates the tracked interface for the Newtonian-Newtonian case displacement at a flowrate of 0.1 ml/min with measurements taken from the onset of the first observable instability for a total of 5 s ( $t_{max} = 5$  s). By using the velocity of the displacement front and the distance from the measuring window to the channel bend, the time required for the displacement front to reach the first bend was calculated and noted with a red line on Fig. 9(i). Given the U-bend configurations of the microchannel after the initial straight section, it is expected that the shape of the interface will be affected by additional perturbations from the backwave when the displacement front reaches the bend. The backwave from the bend will

affect the interfacial instabilities and will increase the complexity of the interfacial shape; this will be further discussed in the next section.

To better understand the evolution of the instabilities, one dimensional continuous wavelet transformation (1D CWT) was performed, which provides information on the frequencies and amplitudes of the interfacial waves and their evolution over the recording time. The results are presented as scalograms of frequency against time with amplitudes shown by the colour spectrum<sup>56,57</sup>. The scalogram for the mean interfacial displacement data of the Newtonian-Newtonian fluid pair are shown in Fig. 9(ii) for the same interfacial data in Fig. 9(i), for a displacing flowrate of 0.1 ml/min.

Two main modes of instability are seen in the scalogram. The first instability mode, M1, is related to the slow shift of the aqueous core at a low frequency of around 1 Hz throughout the entire recording time. The aqueous core migrates between the top and the bottom of the channel without directly contacting the wall, while the residual organic film remains continuous as seen in the first inset in Fig. 9(ii). Off-centre core shift is the primary mode of instability seen in all Newtonian-Newtonian fluid displacements. This migration minimises the overall drag force experienced by the aqueous core, in qualitative agreement with studies conducted previously<sup>11,54,55</sup>. When the core is off centre, the hydrostatic force imbalance between the top and the bottom part of the channel causes the core to move between the two positions, at a frequency of 1 Hz in this study.

The second mode of instability, M2, occurred at higher frequencies between 5 to 10 Hz. This instability is the result of the exponential growth of the small perturbations introduced at the entrance, as well as of the backwave from the channel bend. From the interfacial data in Fig. 9(i), it can be seen that these instabilities are non-periodic, and their frequencies and amplitudes vary over time. The interfacial waves are not consistent, and the instabilities may appear as 'bursts' of waves in short succession. An example of mode M2 is shown circled by a dash line in Fig. 9(i) with the accompanying frequencies in Fig. 9(ii), whereby a single large interfacial wave is observed at about  $t/t_{max} = 0.6$  with no obvious periodic repetition. The second inset of Fig. 9(ii) shows the image sequences of an M2 instability.

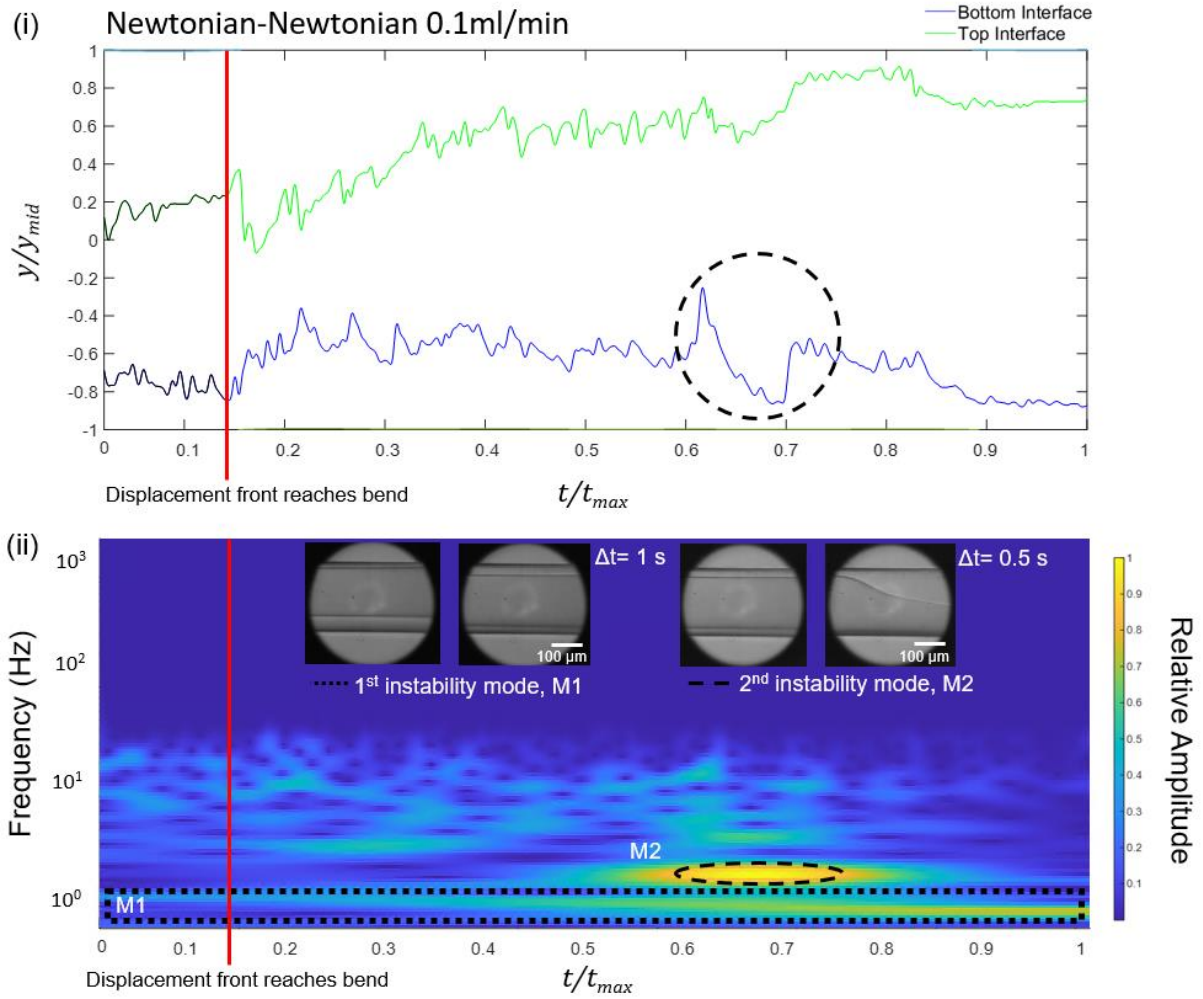


**Fig. 9.** (i) Dimensionless Newtonian-Newtonian displacement interface tracking data at a displacing flowrate of 0.1 ml/min. (ii) Mean interface scalogram of the interfacial instability for the Newtonian-Newtonian displacement at a flowrate of 0.1 ml/min. Red line shows the time taken for the displacement front to reach the first channel bend, dotted square indicates the first instability mode, M1, and black dashed circle indicates an example of a large instability (second instability mode, M2). Inset: Image sequences of first and second instability modes.  $\Delta t$  indicates the time between the two images.

#### D. Interfacial instabilities tracking for Boger-Newtonian displacement

When the displacing phase was replaced with a Boger fluid, large differences on the interface instabilities were observed when compared to the Newtonian-Newtonian case. Fig. 10(i) illustrates the tracked interface for the Boger-Newtonian fluid pair for a displacing phase flowrate of 0.1 ml/min. Compared to the Newtonian displacing fluid (Fig. 9(i)), the Boger displacing phase produces periodic interfacial instabilities. The scalogram for this tracked interface is shown in Fig. 10(ii). Two modes of instability are still observed, with mode M1 now at around 1.5 Hz. However, the second mode of instability for the Boger-Newtonian case is different to the Newtonian-Newtonian one. Mode M2 is now periodic, both before and after the displacement front reaches the microchannel bend, and its amplitude is sustained throughout the measurement. In Fig. 10(ii), one can observe ‘holes’ within the M2 instability frequency

range, and this usually suggests the combination of at least two frequencies that make up the frequency band<sup>56,57</sup>. For the displacement at 0.1 ml/min, the average frequency of the M2 mode was 4.2 Hz, with an average amplitude of 12  $\mu\text{m}$  when measured from crest to crest and crest to trough respectively.

The periodicity of M2 can be attributed to the elastic behaviour of the displacing phase when the Weissenberg number is larger than 1. In all the Boger-Newtonian displacement experiments,  $Wi$  varies between  $Wi = 4.2$  and  $Wi = 21$ , as the Boger fluid has a relaxation time ( $\lambda = 0.063\text{ s}$ ) longer than the process characteristic time ( $0.002 < \tau < 0.02$ ). As a result, the displacing liquid does not have time to relax and the instabilities maintain their frequency and amplitude (first region in Fig. 10(i)) until they are affected by the backwave from the bends. The effect of bends is discussed in detail in the next section.

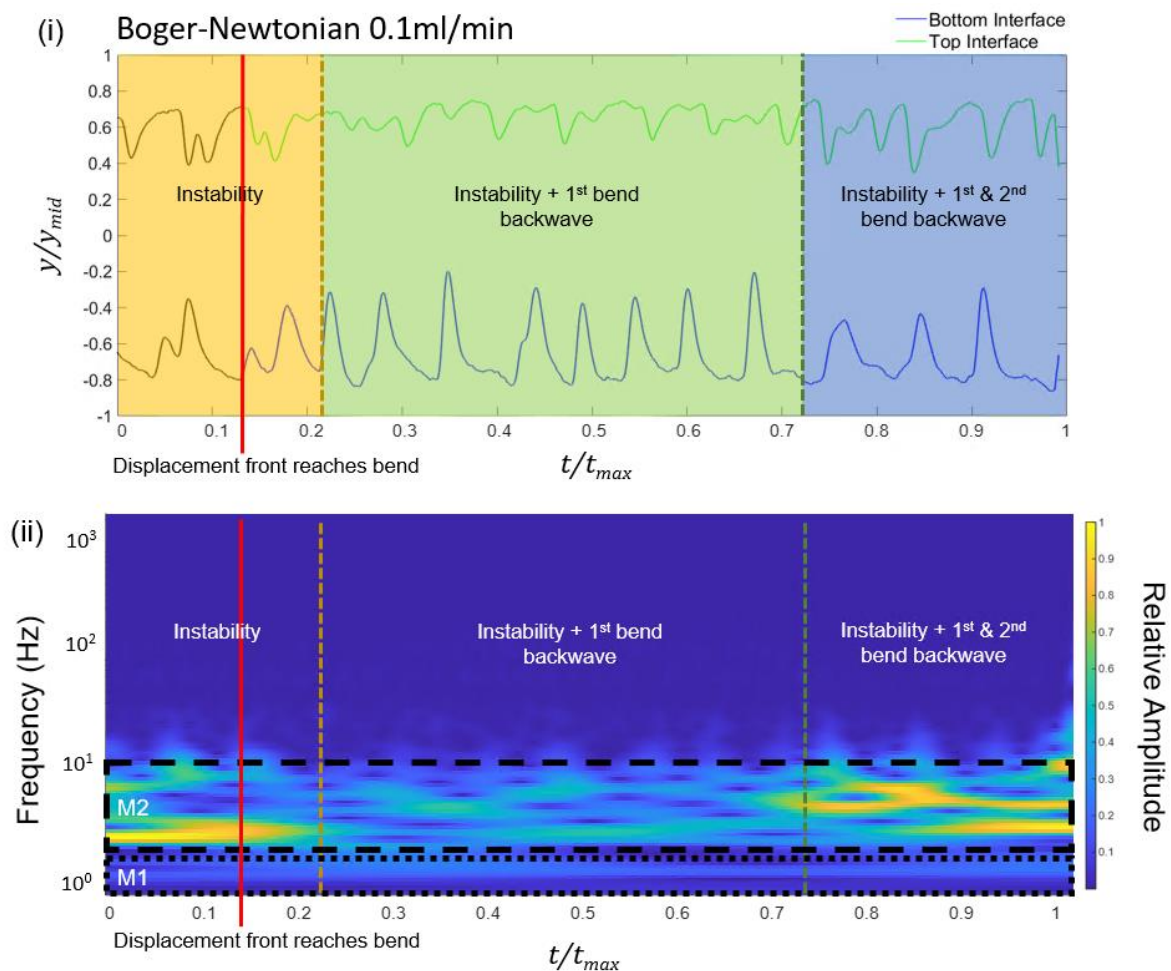


**Fig. 10.** (i) Dimensionless Boger-Newtonian displacement interface tracking data at a displacing flowrate of 0.1 ml/min. (ii) Mean interface scalogram of the interfacial instability for the Boger-Newtonian displacement at a flowrate of 0.1 ml/min. Red line shows the time taken for the displacement front to reach the first channel bend. Three regions with different wave patterns are identified, due to backwave perturbations when the displacement front reaches a bend.

### E. Effects of downstream bend and increasing displacing phase flowrate on interfacial instabilities.

For the Newtonian-Newtonian displacement presented in Fig. 9, there were no major differences in the instabilities before and after the displacement front reaches the bend. The backwaves from the bend only further contributed to the perturbations and the effect of the backwave alone cannot be separated from the rest of the unstable interface. For the case of the Boger-Newtonian displacement however (Fig. 10(i)), the instability is periodic, and it would be possible to isolate the effects of the bends.

Although the exact propagation speed of the backwave from the bend cannot be calculated, as an estimate it can be taken equal to the displacement front speed. This means that a difference on the instability pattern should be seen at approximately twice the time it takes for the displacement front to reach the bend. Based on this, in Fig. 10(i), three regions of different periodic wave patterns were identified for the Boger-Newtonian displacement pair at 0.1 ml/min. The first region ( $t/t_{max} \in [0, 0.2]$ ) is attributed purely to the unstable displacement flow. The second region ( $t/t_{max} \in [0.2, 0.7]$ ) showed the interfacial waves due to the unstable displacement flow with the additional backwaves from the first bend. The backwave changes the shape of the instability from double peaks to a single peak and doubles the largest peak frequency from 2 Hz to 4Hz. As the displacement front reaches the second bend at  $t/t_{max} = 0.7$ , additional perturbations from the second bend are introduced into the flow, changing the shape of the interface again, this time reducing the peak amplitude but further increasing the frequency.

Further investigation on the instabilities for different flowrates of the displacing phase for the Boger-Newtonian case can be seen in Fig. 11. For each case, different regions are identified when backwaves are introduced into the interface instability; for the displacing flowrate of 0.05 ml/min, only 2 regions are observed while at 0.2 ml/min, 4 regions are identified within the 5 seconds of the measurement time.

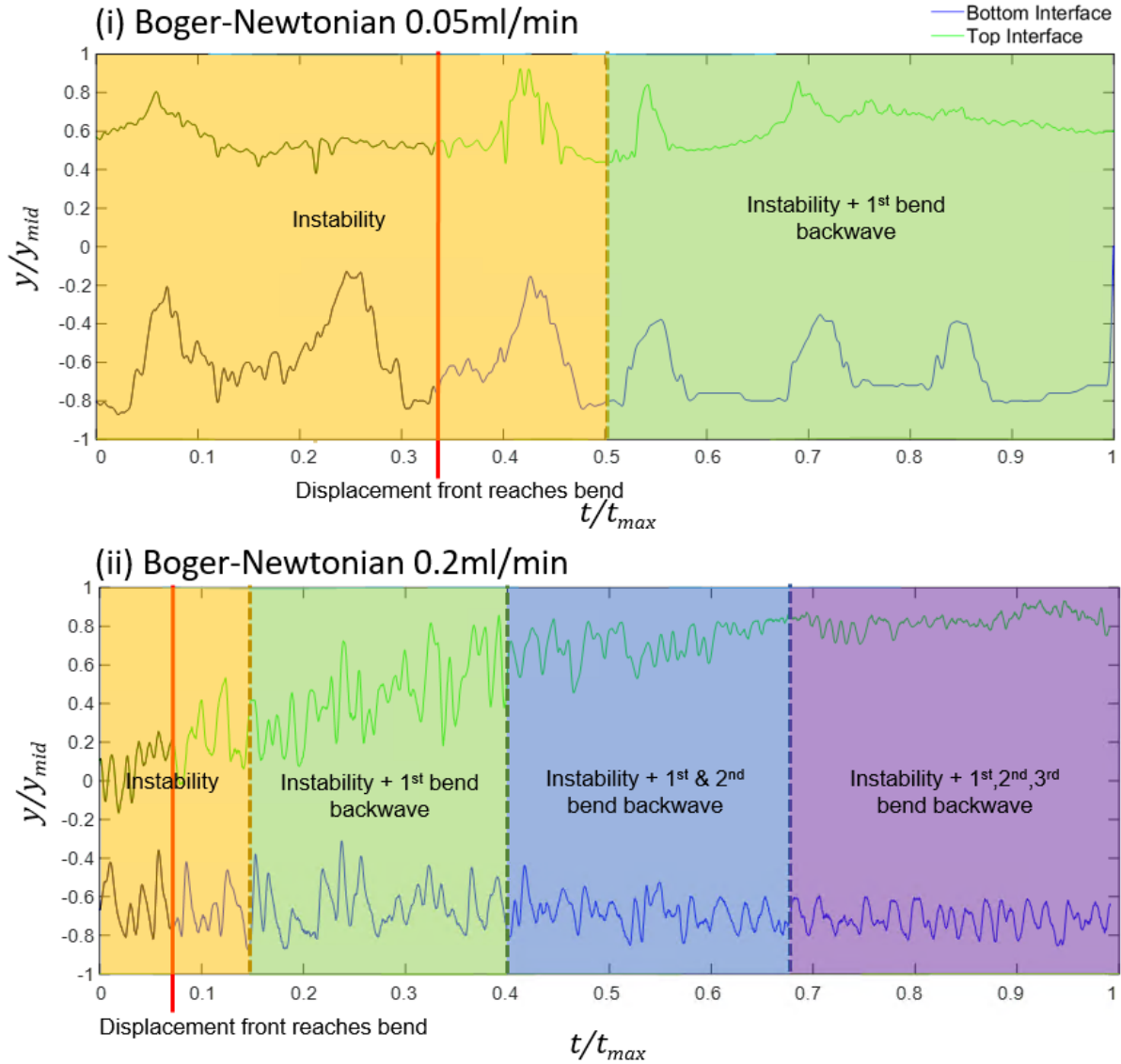


**Fig. 11.** Dimensionless Boger-Newtonian displacement interface tracking data at a displacing flowrate of (i) 0.05 ml/min (ii) 0.2 ml/min. Red line shows the time taken for the displacement front to reach the first channel bend. Multiple regions with different wave patterns are identified, due to backwave perturbations when the displacement front reaches a bend.

To further investigate the effect of the fluid elasticity on the interfacial instability with increasing flowrate, scalograms were produced only for the first region, where there is no interference from the backwaves caused by the bends (Fig. 12). The time here has been normalised with the time taken for the instability front to reach the first bend ( $t/t_{bend}$ ). In each scalogram, bands of frequencies along the time axis are observed, rather than a single frequency island as seen previously in the Newtonian-Newtonian case. This means that the secondary instability mode is the product of superposition of multiple sinusoidal waves, with the first mode of instability still observed at around 1.5 Hz at each flowrate (first frequency band from the bottom in each scalogram). Additionally, for an increasing flowrate of the displacing phase, the number of bands increases, with an overall shift towards higher frequencies. For example, at the

displacing flowrate of 0.05 ml/min, 3 frequency bands, including one for the first instability mode are observed in Fig. 12(i). When the flowrate is increased to 0.1 ml/min, 4 frequency bands are seen, with an increase in the mean frequency (Fig. 12(ii)). Likewise, at the highest displacing flowrate tested, the number of frequency bands increases to 7, with the highest frequency band at 20 Hz (Fig. 12(iii)). A summary of the mean frequencies, ( $f_{mean}$ ) of the second instability mode calculated from the weighted mean of each frequency band, and its corresponding mean amplitudes ( $A_{mean}$ ) is given in Table III.

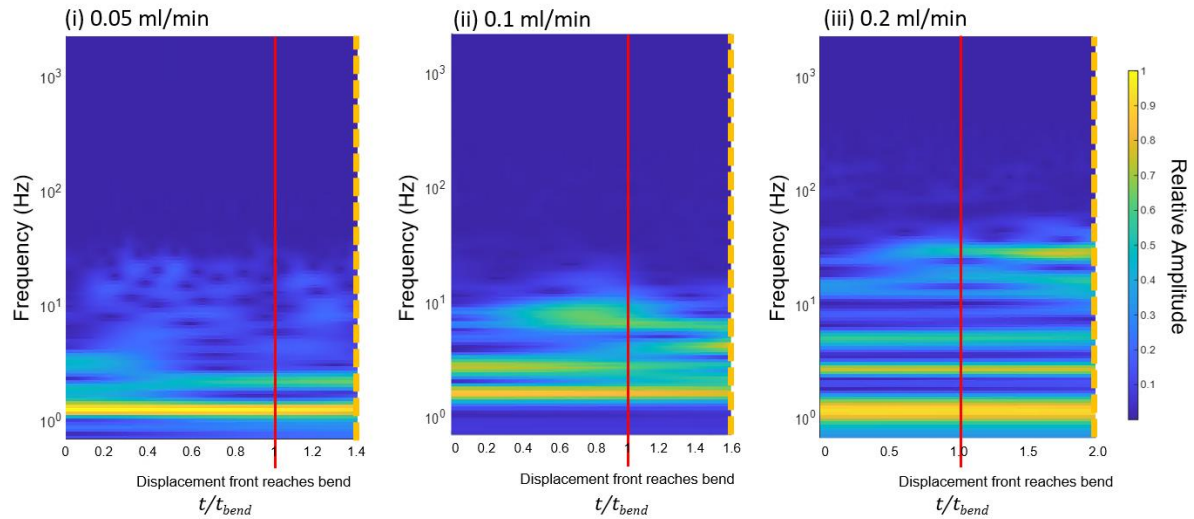


**Fig. 12.** Scalograms of the first region, before backwave perturbations, on the interfacial instability for the Boger-Newtonian displacement fluid pair at (i) 0.05 ml/min (ii) 0.1 ml/min (iii) 0.2 ml/min

**Table III.** Summary of results for the displacement of Boger-Newtonian fluid pair, from  $t = 0$  to  $t = t_{bend}$ .

Displacing Flowrate (ml/min)	$Re$ (-)	$Ca$ (-)	$Wi$ (-)	$f_{mean}$ (Hz)	$A_{mean}$ ( $\mu\text{m}$ )
0.05	0.119	0.015	4.581	2	15
0.1	0.301	0.038	11.590	4.2	12
0.2	0.545	0.068	21.027	10	10

As the flowrate of the displacing phase increases, the Weissenberg number increases as the characteristic time of the flow decreases. There is also an increase in the inertial effects reflected in the increasing Reynolds number, while the flow remains laminar. The increase in the frequency of the second mode of instability with increasing inertial effects was also seen for a Newtonian-Newtonian displacement by Lu et al.<sup>13</sup>. In the case of the Boger-Newtonian displacement, the increase in flowrate dampens the amplitude of the instability; the periodicity, however, remains.

## IV. Conclusions

In this paper, the displacement of an organic liquid by an immiscible aqueous phase was considered inside a microchannel. The displacing phase was a pure viscoelastic liquid (Boger fluid) while the results were compared with those from a Newtonian displacing liquid of the same density and viscosity. The experimental results showed that a viscoelastic displacing phase reduced the residual film thickness on the channel wall when compared to a Newtonian one at high flowrates, thus increasing the displacement efficiency. Correlations for the film thickness were proposed for both the Newtonian-Newtonian and the Boger-Newtonian fluid pairs. The interfacial instabilities that were formed behind the initial displacement front were further investigated. A simple stability analysis showed that the displacement flow is always unstable under the conditions used in this study. Due to the additional elastic stresses, the interfacial instability is observed much earlier when a Boger displacing fluid was used, when compared to a Newtonian one at low flowrates, while at high flowrates there was no significant difference in the onset between the two cases. Different instability patterns were observed, and the instability frequencies were measured. Two modes of instability were found: a low frequency one attributed to core-shifting and a higher frequency one attributed to the viscosity stratification of the two phases across the interface. In all the Boger-Newtonian case experiments, the Weissenberg number was greater than one, resulting in a periodic instability compared to the Newtonian-Newtonian case. As the flowrate increased, the frequency of this instability increased, but the amplitude decreased, because of the increased importance of inertial effects. The effects of bends in the microchannel were also briefly investigated, and the changes in the interfacial wave pattern due to the superposition of the backwaves from the bends were identified.

The small initial residual film when a viscoelastic liquid is used could increase the overall efficiency in channel cleaning or in EOR applications by displacement. Also, understanding the instability pattern after the displacement front could help to ensure maximum displacement efficiency. With the viscoelastic liquid, the earlier onset of instabilities and the larger amplitude of the travelling waves, when compared to the Newtonian liquid, would result in efficient removal of the initial liquid. In the future, we will study the velocity fields in the two phases with particle image velocimetry to better understand the effects of viscoelasticity on the displacement phenomena in small channels.



## Authors Contribution

**Seng Hoe Hue:** Conceptualization, Investigation, Methodology, Project administration, Data curation, Visualization, Writing - original draft, Software, Formal analysis. **Loïc Chagot:** Writing – review & editing, Validation. **Panagiota Angeli:** Supervision, Writing -review & editing, Resources, Conceptualization, Funding acquisition.

## Declaration of Competing Interest

The authors declare that they have no known competing financial interests or personal relationships that could have appeared to influence the work reported in this paper.

## Acknowledgement

The authors would like to acknowledge support from the UK Engineering and Physical Sciences Research Council (EPSRC) Programme Grant PREMIERE (EP/T000414/1). S Hue would also like to acknowledge Petroliam Nasional Berhad (PETRONAS) for his studentship.

## Appendix/ Supplementary Material

### A. Linear stability analysis

The following procedure for a linear stability analysis is similar to the one employed by Foroughi et al.<sup>11</sup> and Funada and Joseph<sup>53</sup>. Here, the organic phase, denoted by subscript  $o$  and the aqueous phase, denoted by subscript  $aq$  is used. The scaling parameters used to non-dimensionalised the Navier-Stokes equation are as follow: characteristic length,  $R^* = D/2$ , characteristic velocity,  $W^* = \sqrt{\frac{\sigma}{\rho_o R}}$ , and characteristic pressure,  $P^* = \rho_o W^{*2}$ . And the following dimensionless quantity are obtained: dimensionless velocity,  $U = V/W^*$ , dimensionless pressure,  $P = p/P^*$ , dimensionless radius,  $r = r/R^*$  and dimensionless time,  $t = TW^*/r$ . Additionally, the viscosity ratio,  $m = \rho_{aq}/\rho_o$ ; density ratio,  $l = \rho_{aq}/\rho_o$  and modified Reynolds number,  $Re^* = \frac{\rho_o W^* R^*}{\mu_o}$  are used. The general scaling term used to non-dimensionalised partial differential equations is shown in Equation A1.

$$\frac{\partial^n x}{\partial t^n} = \frac{x_s}{t_s^n} \frac{\partial^n \bar{x}}{\partial \bar{t}^n} \quad (A1)$$

Starting from the Navier-Stokes equation in cylindrical coordinate for both phases and considering flow only in the axial direction,  $z$ , the following equations are obtained for the dimensionless momentum equation:

$$l \left( \frac{\partial U_{aq}}{\partial t} + U_{aq} \frac{\partial U_{aq}}{\partial z} \right) = - \frac{dP_{aq}}{dz} + \frac{m}{Re^*} \frac{1}{r} \frac{\partial}{\partial r} \left( r \frac{\partial U_{aq}}{\partial r} \right) \quad (A2)$$

$$\frac{\partial U_o}{\partial t} + U_o \frac{\partial U_o}{\partial z} = - \frac{dP_o}{dz} + \frac{1}{Re^*} \frac{1}{r} \frac{\partial}{\partial r} \left( r \frac{\partial U_o}{\partial r} \right) \quad (A3)$$

For the aqueous and organic phase respectively. In the case of our test fluid,  $Re^* = 2.06$ ,  $l = 1.146$  and  $m = 0.82$ .

For a laminar annular flow, the velocity profiles of both phases are

$$U_{aq} = \bar{U}_{aq} \frac{(a - r^2) + m(1 - a^2)}{a^2 + m(1 - a^2)}, \quad 0 \leq r \leq a \quad (A4)$$

$$U_o = \bar{U}_o \frac{r^2 - 1}{\frac{1}{2}(a^2 - 1)}, \quad a \leq r \leq 1 \quad (A5)$$

where  $\bar{U}$  is the average dimensionless velocity for the cross section of the channel. At the interface, the velocity between the two phases are the same, i.e.,  $U_{aq} = U_o$  at  $r = a$  and the relationship between the velocity of the aqueous and organic phase can be calculated. To By substituting the velocity profiles (Equation A4 and A5) into Equation A2 and A3 respectively and multiplying the equation with  $rdr$ , the Navier-stokes equations for both phases can then be integrated to obtain the average velocity change with radius, simplifying the analysis.

Substituting Equation A4 into Equation A2, multiplying by  $rdr$  and integrating between  $r = 0$  and  $r = a$  yields

$$l \frac{\partial}{\partial t} \left( \bar{U}_{aq} \frac{a^2}{2} \right) + \frac{1}{2} l \frac{\partial}{\partial z} \left( \bar{U}_{aq}^2 \frac{a^2}{2} \right) = - \frac{dP_{aq}}{dz} \left( \frac{a^2}{2} \right) + \frac{m}{Re^*} \bar{U}_{aq} \left( - \frac{2a^2}{m(a - a^2) + \frac{a^2}{2}} \right) \quad (A6)$$

Similarly, substituting Equation A5 into Equation A3, multiplying by  $rdr$  and integrating between  $r = a$  and  $r = 1$  yields

$$\frac{\partial}{\partial t} \left( \bar{U}_o \frac{1 - a^2}{2} \right) + \frac{1}{2} \frac{\partial}{\partial z} \left( \bar{U}_o^2 \frac{1 - a^2}{2} \right) = - \frac{dP_o}{dz} \left( \frac{1 - a^2}{2} \right) - \frac{4}{Re^*} \bar{U}_o \quad (A7)$$

The mass balance equation for both phases then become,

$$-\frac{d}{dz}(\bar{U}_{aq}a^2) = \frac{d}{dt}(a^2) \quad (A8)$$

$$\frac{d}{dz}\bar{U}_o(1-a^2) = \frac{d}{dt}(a^2) \quad (A9)$$

In the experimental setup, perturbations are introduced in the form of velocity fluctuations from the syringe pump and the valves. This can be introduced into the stability analysis as perturbations in the axial direction (denoted by primes),

$$a' = a_0 \varepsilon e^{\omega t + ikz} \quad (A10)$$

$$\bar{U}'_{aq} = \varepsilon v_{aq} e^{\omega t + ikz} \quad (A11)$$

$$\bar{U}'_o = \varepsilon v_o e^{\omega t + ikz} \quad (A12)$$

Where  $a_0$  is the initial dimensionless interfacial position,  $\omega$  is the dimensionless growth rate,  $k$  is the dimensionless wave number (equals to  $\frac{2\pi}{\theta}$ , where  $\theta$  is the dimensionless wavelength).  $v_{aq}$  and  $v_o$  are dimensionless term in terms of  $\omega$ ,  $a_0$  and  $\theta$  from substituting Equation A10-A12 into the mass balance equation (Equation C8 and C9).

The perturbed dimensionless normal stresses are the same at the interface, where

$$\frac{\partial}{\partial z}(P'_{aq} - P'_o) = -\frac{1}{We^*} \frac{\partial}{\partial z} \left( \frac{a'}{a_0^2} + \frac{\partial^2 a'}{\partial z^2} \right) \quad (A13)$$

$We^*$  is the Weber number based on the characteristic velocity ( $We^* = \frac{\rho_o W^{*2} R}{\sigma}$ ), and is assumed to be unity. The perturbations terms are substituted into Equation A6, A7 and A13, with Equation A6 and A7 combined into a single equation using Equation A13. Ignoring terms higher than the second order, imaginary terms, and the inertia term (terms with  $Re$ ), the single equation resembles a simple quadratic equation with respect to  $\omega$ .

$$A\omega^2 + B\omega + C = 0 \quad (A14)$$

With

$$A = 2 \left( l + \frac{a_0^2}{1 - a_0^2} \right) \quad (A15)$$

$$B = \frac{8}{Re^*} \left[ \frac{2a_0^2}{(1 - a_0^2)} + \frac{m}{\left(m(1 - a_0^2) + \frac{a_0^2}{2}\right)} \right] \quad (A16)$$

$$C = \frac{1}{We^*} \left[ a_0 k^4 - \left(\frac{1}{a_0}\right) k^2 \right] \quad (A17)$$

Solving Equation A14 will thus yield the growth rate of perturbations introduced, as seen in Fig. 6.

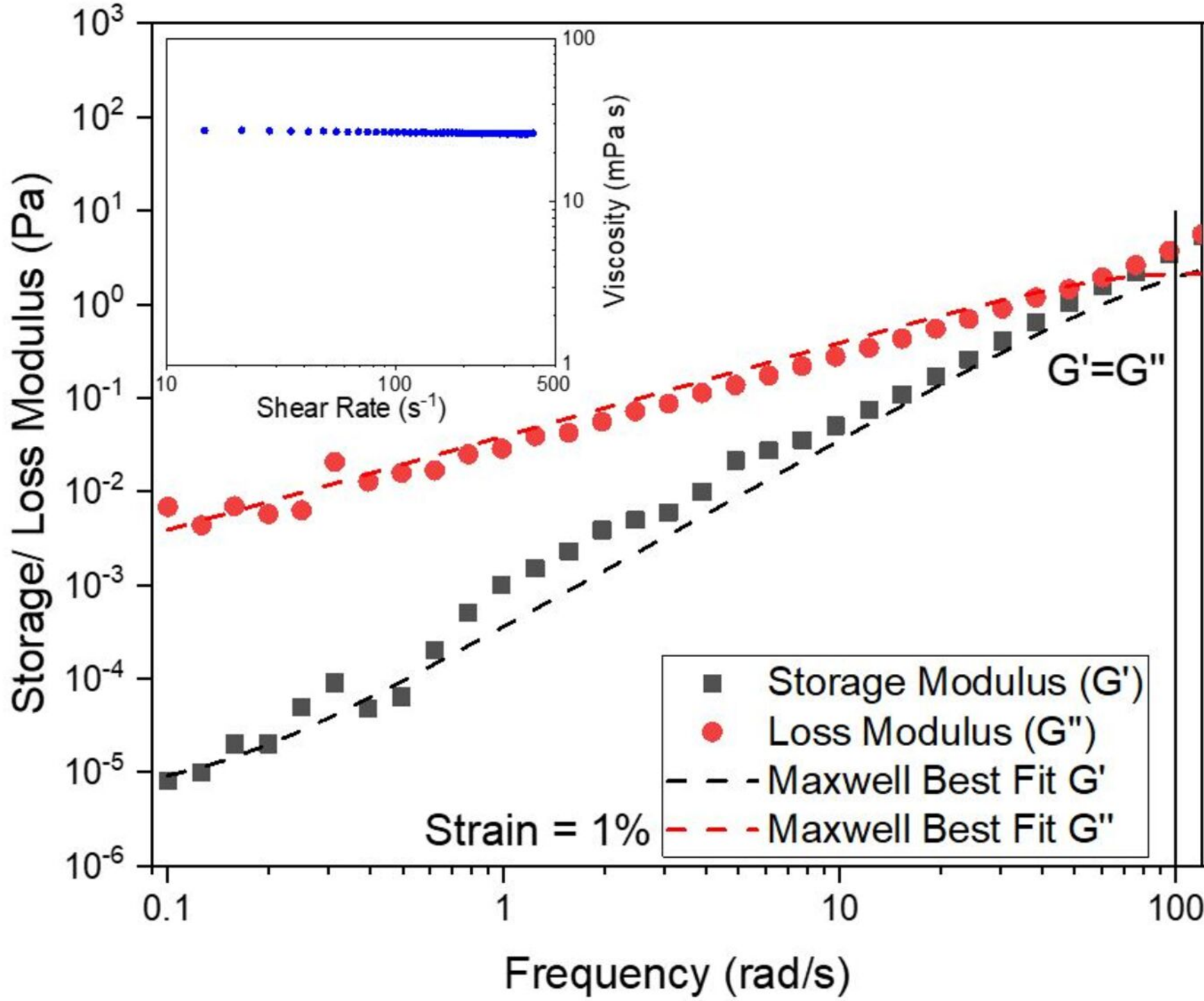
## References

- <sup>1</sup> Taylor, G. I. Deposition of a viscous fluid on the wall of a tube. *Journal of Fluid Mechanics* **10**, 161–165 (1961).
- <sup>2</sup> Guha, A., Barron, R. M. & Balachandar, R. An experimental and numerical study of water jet cleaning process. *Journal of Materials Processing Technology* **211**, 610–618 (2011).
- <sup>3</sup> Yang, B., Lian, K., Zhao, Y., Zhu, J. & Guo, A. Research on automatic cleaning equipment with high pressure water jet for optical pipelines. in *Journal of Physics: Conference Series* vol. **1654**, 012095(1)-012095(10)
- <sup>4</sup> Massarweh, O. & Abushaikha, A. S. The use of surfactants in enhanced oil recovery: A review of recent advances. *Energy Reports* **6**, 3150–3178 (2020).
- <sup>5</sup> Mahon, R., Oluyemi, G., Oyeneyin, B. & Balogun, Y. Experimental investigation of the displacement flow mechanism and oil recovery in primary polymer flood operations. *SN Applied Sciences* **3**,1-19 (2021).
- <sup>6</sup> Hewitt, G. F. & Hall-Taylor, N. S. *Annular two-phase flow*. (Pergamon Press, Oxford, New York, 1970).
- <sup>7</sup> Mandhane, J. M., Gregory, G. A. & Aziz, K. A flow pattern map for gas-liquid in horizontal pipes. *International Journal of Multiphase Flow* **1**, 537–553 (1974).
- <sup>8</sup> Weisman, J., Duncan, D., Gibson, J. & Crawford, T. Effects of fluid properties and pipe diameter on two-phase flow patterns in horizontal lines. *International Journal of Multiphase Flow* **5**, 437–462 (1979).
- <sup>9</sup> Bai, R., Chen, K. & Joseph, D. D. Lubricated pipelining: Stability of core—annular flow. Part 5. Experiments and comparison with theory. *Journal of Fluid Mechanics* **240**, 97–132 (1992).
- <sup>10</sup> Soares, E. J., Carvalho, M. S. & Souza Mendes, P. R. Immiscible liquid-liquid displacement in capillary tubes. *Journal of Fluids Engineering* **127**, 24–31 (2005).
- <sup>11</sup> Foroughi, H., Abbasi, A., Das, K. S. & Kawaji, M. Immiscible displacement of oil by water in a microchannel: Asymmetric flow behavior and nonlinear stability analysis of core-annular flow. *Physical Review* **85**, 026309(1)-026309(10) (2012).
- <sup>12</sup> Lu, Y. B., Tang, G. H. & Tao, W. Q. Experimental study of microchannel flow for non-Newtonian fluid in the presence of salt. *Experimental Thermal and Fluid Science* **74**, 91–99 (2016).

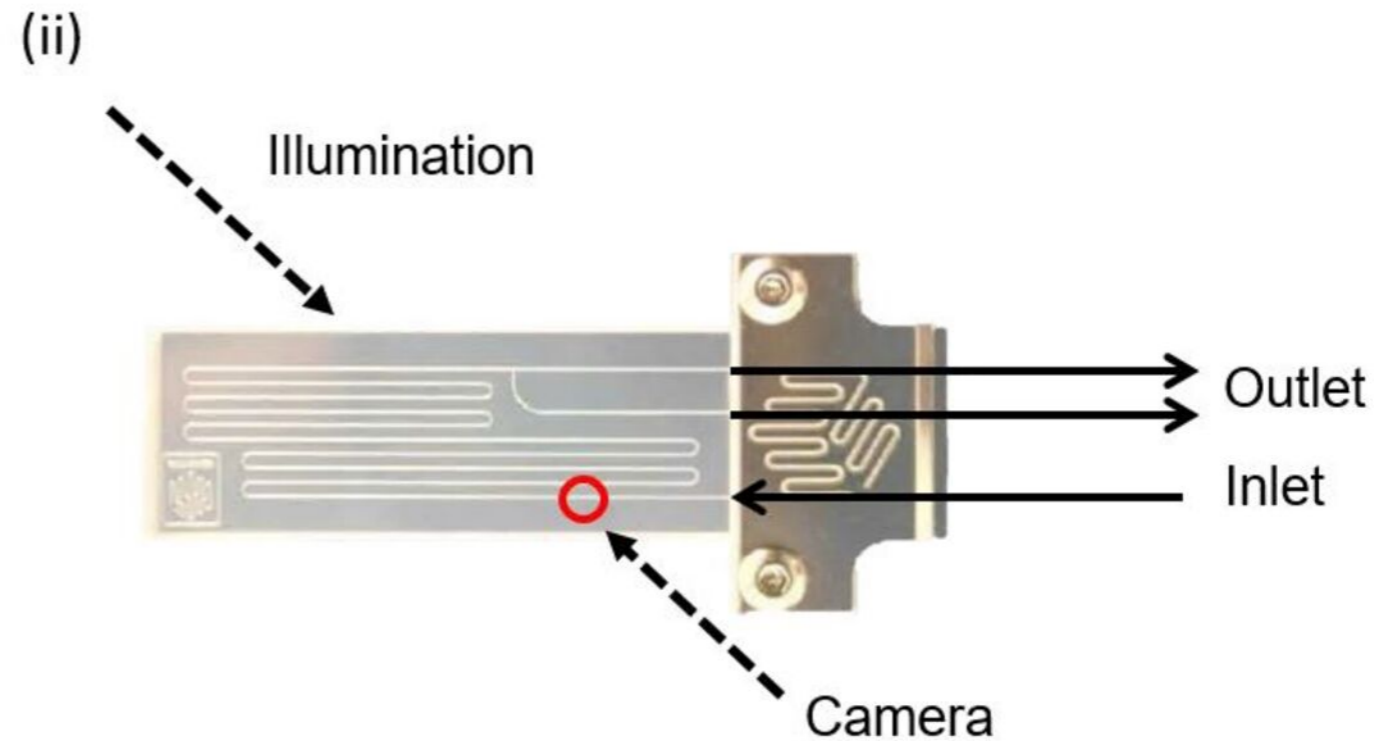
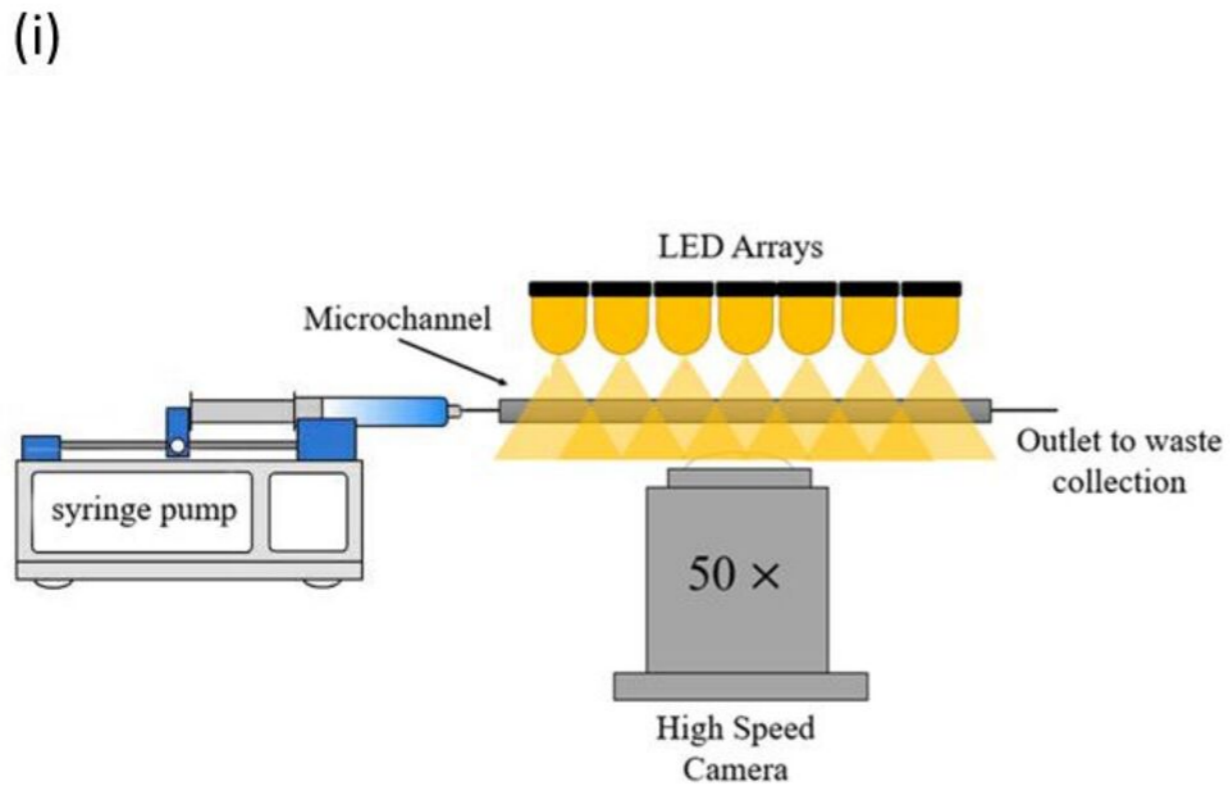
- <sup>13</sup> Lu, Y., Kovalchuk, N. M., Che, Z. & Simmons, M. J. H. Interfacial instabilities due to immiscible fluid displacement in circular and non-circular microchannels. *Experimental Thermal and Fluid Science* **113**, 11045(1)-11045(11) (2020).
- <sup>14</sup> De, S. *et al.* Viscoelastic effects on residual oil distribution in flows through pillared microchannels. *Journal of Colloid and Interface Science* **510**, 262–271 (2018).
- <sup>15</sup> Gogoi, S. & Gogoi, S. B. Review on microfluidic studies for EOR application. *Journal of Petroleum Exploration and Production Technology* **9**, 2263–2277 (2019).
- <sup>16</sup> Fairbrother, F. & Stubbs, A. E. Studies in Electro-endosmosis. Part VI. The “bubble-tube” Method of Measurement. *J. Chemical Society* 527–529 (1935).
- <sup>17</sup> Marchessault, R. N. & Mason, S. G. Flow of Entrapped Bubbles through a Capillary. *Industrial and Engineering Chemistry* **52**, 79–84 (1960).
- <sup>18</sup> Bretherton, F. P. The motion of long bubbles in tubes. *Journal of Fluid Mechanics* **10**, 166–188 (1961).
- <sup>19</sup> Aussillous, P. & Quere, D. Quick deposition of a fluid on the wall of a tube. *Physics of Fluids* **12**, 2367–2371 (2000).
- <sup>20</sup> Han, Y. & Shikazono, N. Measurement of the liquid film thickness in micro tube slug flow. *International Journal of Heat and Fluid Flow* **30**, 842–853 (2009).
- <sup>21</sup> Boomkamp, P. A. M. Stability of parallel two-phase flow. (1998).
- <sup>22</sup> Saffman P. G. & Taylor Geoffrey. The penetration of a fluid into a porous medium or Hele-Shaw cell containing a more viscous liquid. *Proceeding of the Royal Society A* **245**, 312–329 (1958).
- <sup>23</sup> Jha, N. K. & Steinberg, V. Elastically driven Kelvin-Helmholtz-like instability in straight channel flow. *PNAS* **118**, 1–7 (2021).
- <sup>24</sup> Boomkamp, P. A. M. & Miesen, R. H. M. Classification of instabilities in parallel two-phase flow. *International Journal of Multiphase Flow* **22**, 67–88 (1996).
- <sup>25</sup> Charru, F. & Hinch, E. J. “Phase diagram” of interfacial instabilities in a two-layer Couette flow and mechanism of the long-wave instability. *Journal of Fluid Mechanics* **414**, 195–223 (2000).
- <sup>26</sup> Preziosi, L., Chen, K. & Joseph, D. D. Lubricated pipelining: Stability of core-annular flow. *Journal of Fluid Mechanics* **201**, 323–356 (1989).
- <sup>27</sup> Hu, H. H. & Joseph, D. D. Lubricated pipelining: Stability of core-annular flow. part 2. *Journal of Fluid Mechanics* **205**, 359–396 (1989).
- <sup>28</sup> Chen, K., Bai, R. & Joseph, D. D. Lubricated pipelining: Part 3 Stability of core-annular flow in vertical pipes. *Journal of Fluid Mechanics* **214**, 251–286 (1990).
- <sup>29</sup> Joseph, D. D. Lubricated pipelining: Stability of core-annular flow. part 4. ginzburg-landau equations. *Journal of Fluid Mechanics* **227**, 587–615 (1991).
- <sup>30</sup> Aul, R. W. The motion of drops and long bubbles through small capillaries: Coalescence of drops and annular film stability. (1989).
- <sup>31</sup> Aul, R. W. & Olbricht, W. L. Stability of a thin annular film in pressure-driven, low-Reynolds-number flow through a capillary. *Journal of Fluid Mechanics* **215**, 585–599 (1990).
- <sup>32</sup> Scoffoni, J., Lajeunesse, E. & Homsy, G. M. Interface instabilities during displacements of two miscible fluids in a vertical pipe. *Physics of Fluids* **13**, 553–554 (2001).
- <sup>33</sup> Yih, C. S. Instability due to viscosity stratification. *Journal of Fluid Mechanics* **27**, 337–352 (1967).
- <sup>34</sup> Lindner, A., Bonn, D., Poiré, E. C., Amar, M. ben & Meunier, J. Viscous fingering in non-Newtonian fluids. *Journal of Fluid Mechanics* **469**, 237–256 (2002).

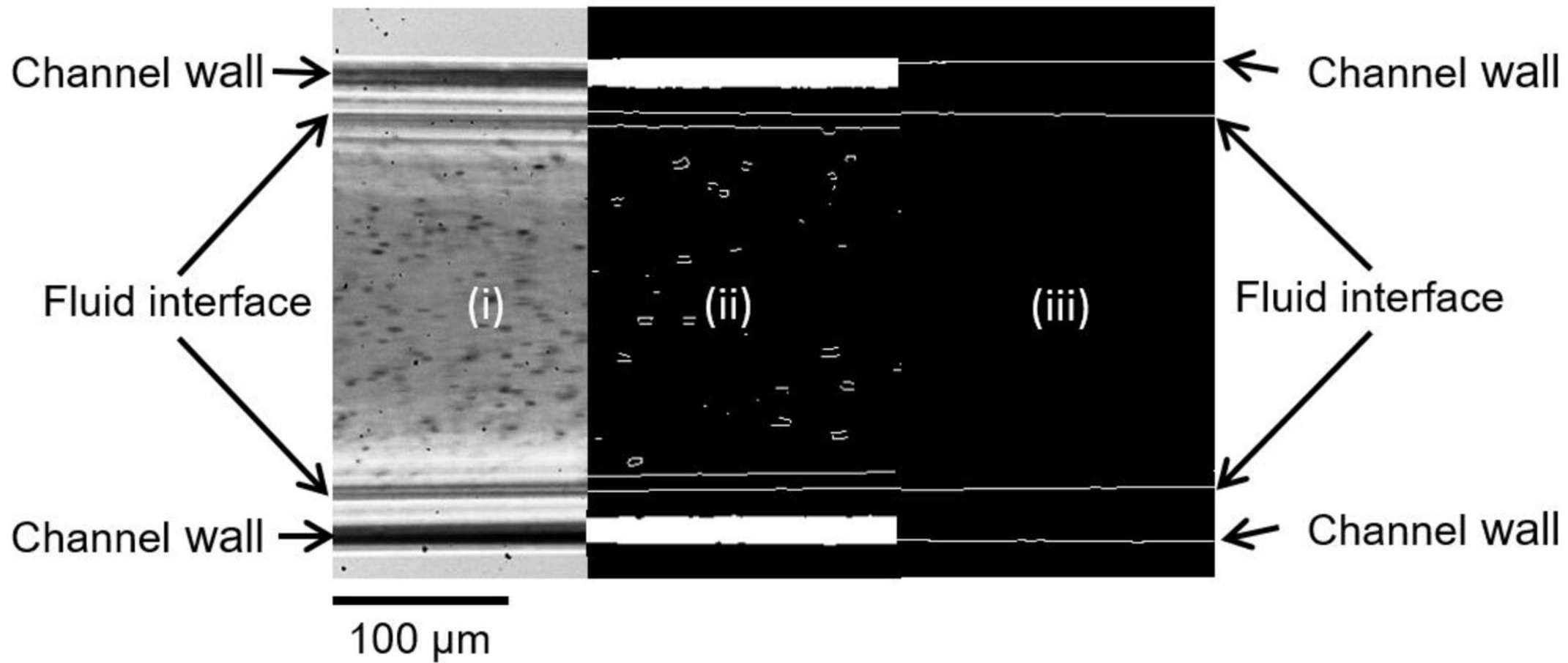
- <sup>35</sup> Gabard, C. & Hulin, J. P. Miscible displacement of non-newtonian fluids in a vertical tube. *European Physical Journal E* **11**, 231–241 (2003).
- <sup>36</sup> Freitas, J. F., Soares, E. J. & Thompson, R. L. Immiscible Newtonian displacement by a viscoplastic material in a capillary plane channel. *Rheologica Acta* **50**, 403–422 (2011).
- <sup>37</sup> Shi, Y. & Tang, G. H. Non-Newtonian rheology property for two-phase flow on fingering phenomenon in porous media using the lattice Boltzmann method. *Journal of Non-Newtonian Fluid Mechanics* **229**, 86–95 (2016).
- <sup>38</sup> Malhotra, S. & Sharma, M. M. Impact of fluid elasticity on miscible viscous fingering. *Chemical Engineering Science* **117**, 125–135 (2014).
- <sup>39</sup> Soori, T. & Ward, T. Stable and unstable miscible displacement of a shear-thinning fluid at low Reynolds number. *Physics of Fluids* **30**, 103101(1)-103101(12) (2018).
- <sup>40</sup> Gauri, V. & Koelling, K. W. Gas-assisted displacement of viscoelastic fluids: flow dynamics at the bubble front. *Journal of Non-Newtonian Fluid Mechanics* **83**, 183–203 (1999).
- <sup>41</sup> Dimakopoulos, Y. & Tsamopoulos, J. On the gas-penetration in straight tubes completely filled with a viscoelastic fluid. *Journal of Non-Newtonian Fluid Mechanics* **117**, 117–139 (2004).
- <sup>42</sup> Fabrízio Quintella, E., Roberto, P., Mendes, S. & Rio, P.-. Displacement of dilute polymer solutions in capillary tube. in *10th Brazilian Congress of Thermal Sciences and Engineering* 0733(1)-0733(10) (2004).
- <sup>43</sup> Saintyves, B., Mora, S. & Bouchaud, E. A meniscus fingering instability in viscoelastic fluids. *Physics of Fluids* **31**, 063108(1)-063108(8) (2019).
- <sup>44</sup> Soares, E. J., De, P. R., Mendes, S., Da, M. & Carvalho, S. Immiscible Liquid-Liquid Displacement in Capillary Tubes: Viscoelastic Effects. *Journal of the Brazilian Society of Mechanical Science and Engineering* **30**, 160–165 (2008).
- <sup>45</sup> Mora, S. & Manna, M. From viscous fingering to elastic instabilities. *Journal of Non-Newtonian Fluid Mechanics* **173–174**, 30–39 (2012).
- <sup>46</sup> Mora, S. & Manna, M. Saffman-Taylor instability of viscoelastic fluids: From viscous fingering to elastic fractures. *Physical Review* **81**, 026305(1)-026305(10) (2010).
- <sup>47</sup> Gan, H. Y., Lam, Y. C., Nguyen, N. T., Tam, K. C. & Yang, C. Efficient mixing of viscoelastic fluids in a microchannel at low Reynolds number. *Microfluidics and Nanofluidics* **3**, 101–108 (2007).
- <sup>48</sup> Dontula, P., Macosko, C. W. & Scriven, L. E. Model Elastic Liquids with Water-Soluble Polymers. *AIChE Journal* **44**, 1247–1255 (1998).
- <sup>49</sup> Boger, D. v. A highly elastic constant-viscosity fluid. *Journal of Non-Newtonian Fluid Mechanics* **41**, 87-91 (1978).
- <sup>50</sup> Balestra, G., Zhu, L. & Gallaire, F. Viscous Taylor droplets in axisymmetric and planar tubes: from Bretherton’s theory to empirical models. *Microfluidics and Nanofluidics* **22**, 67(1)-67(22) (2018).
- <sup>51</sup> Irandoust, S. & Andersson, B. Liquid Film in Taylor Flow through a Capillary. *Industrial and Engineering Chemistry Research* **28**, 1684–1688 (1989).
- <sup>52</sup> Angeli, P. & Gavriilidis, A. Hydrodynamics of Taylor flow in small channels: A review. in *Proceedings of the Institution of Mechanical Engineers, Part C: Journal of Mechanical Engineering Science* vol. **222**, 737–751 (2008).
- <sup>53</sup> Funada, T. & Joseph, D. D. Viscous potential flow analysis of capillary instability. *International Journal of Multiphase Flow* **2002**, 1459–1478 (2002).

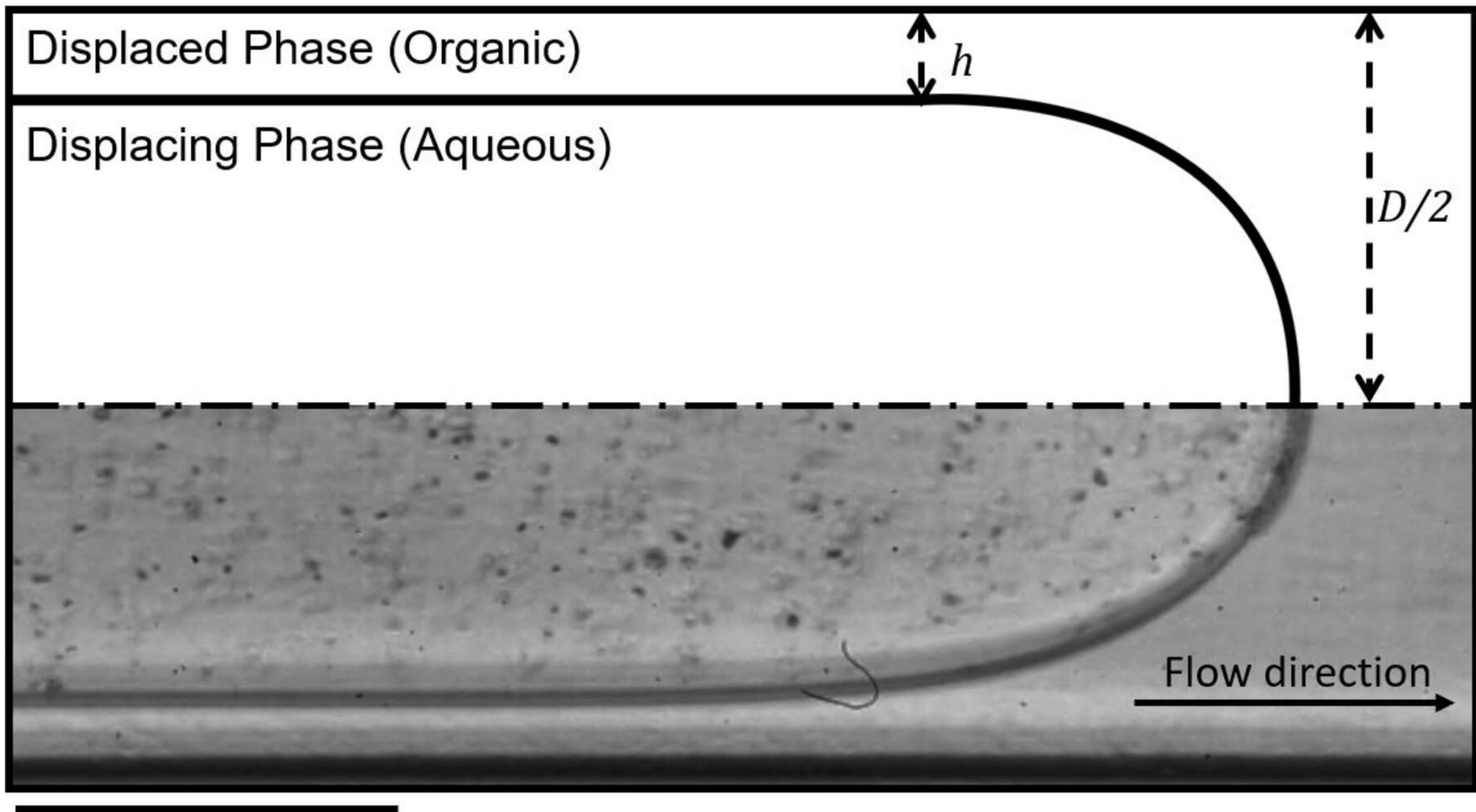
- <sup>54</sup> Tehrani, M. A., Bittleston, S. H. & Long, P. J. G. Flow instabilities during annular displacement of one non-Newtonian fluid by another. *Experiments in Fluids* **14**, 246–256 (1993).
- <sup>55</sup> Tudose, E. T. & Kawaji, M. Experimental investigation of Taylor bubble acceleration mechanism in slug flow. *Chemical Engineering Science* **54**, 5761–5775 (1999).
- <sup>56</sup> Smith, S. W. *The scientist and engineer's guide to digital signal processing*. (California Technical Publishing, 1997).
- <sup>57</sup> Brunton, S. L. & Kutz, J. N. *Data driven science & engineering*. (University of Washington, 2017).





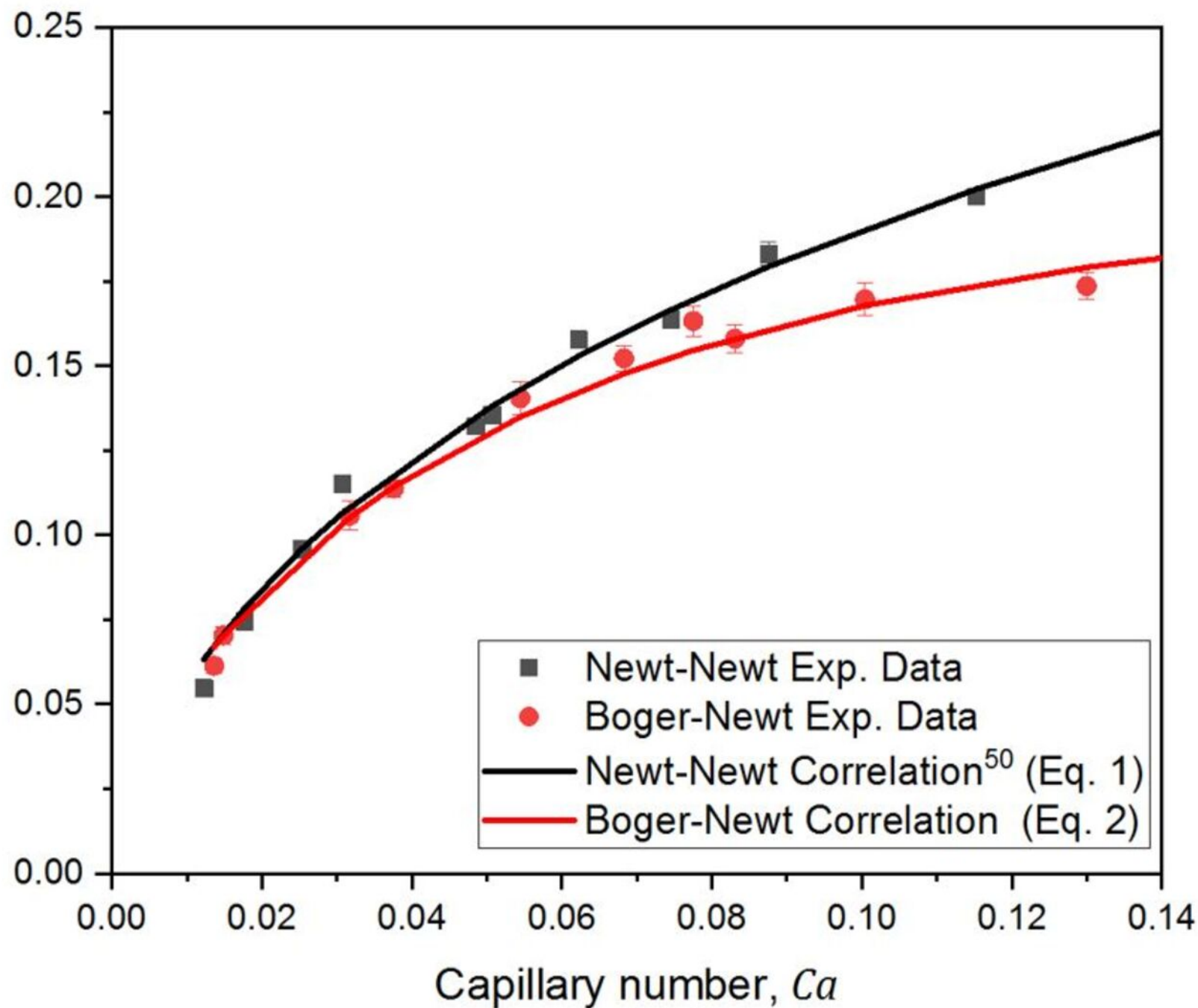


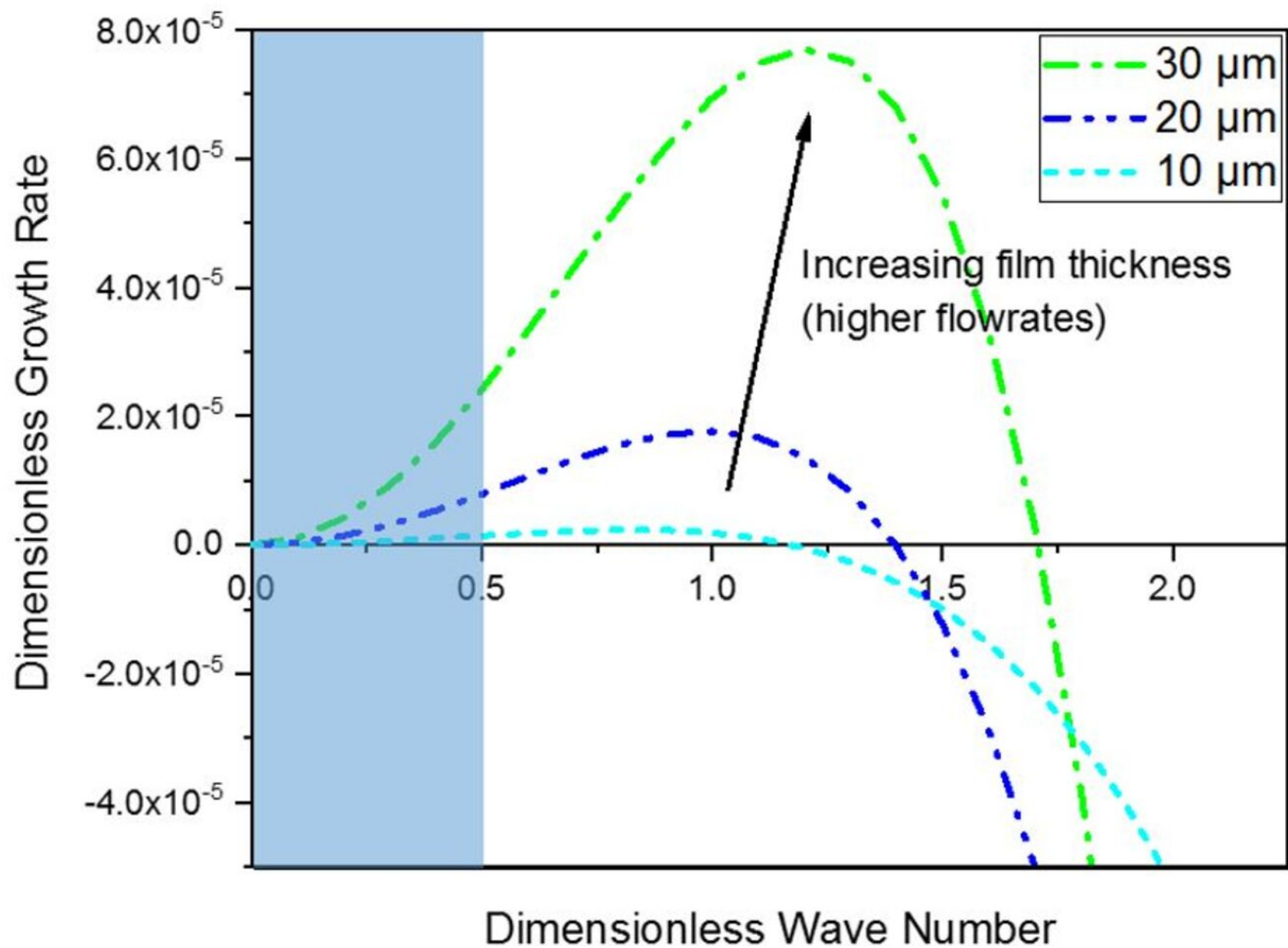


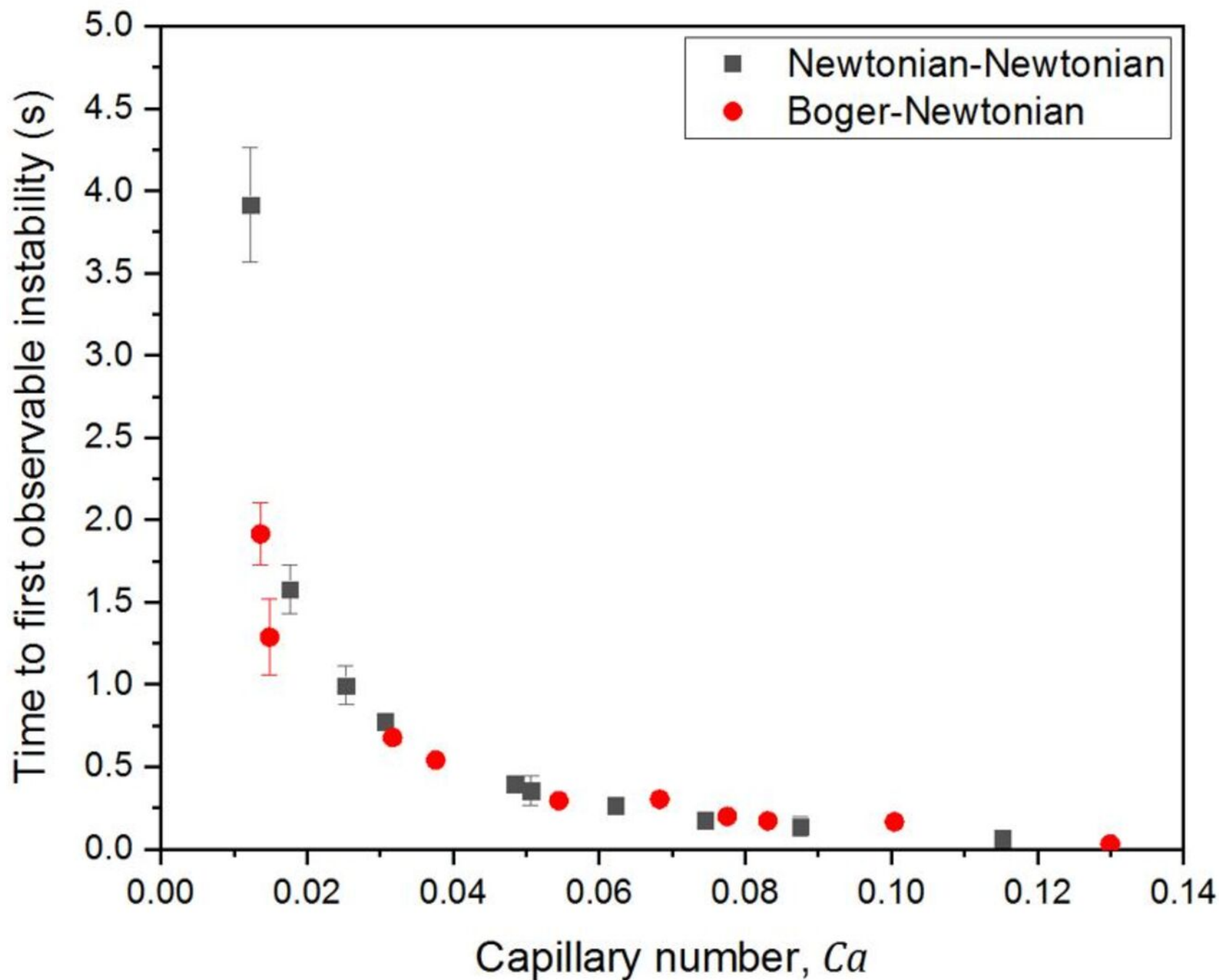


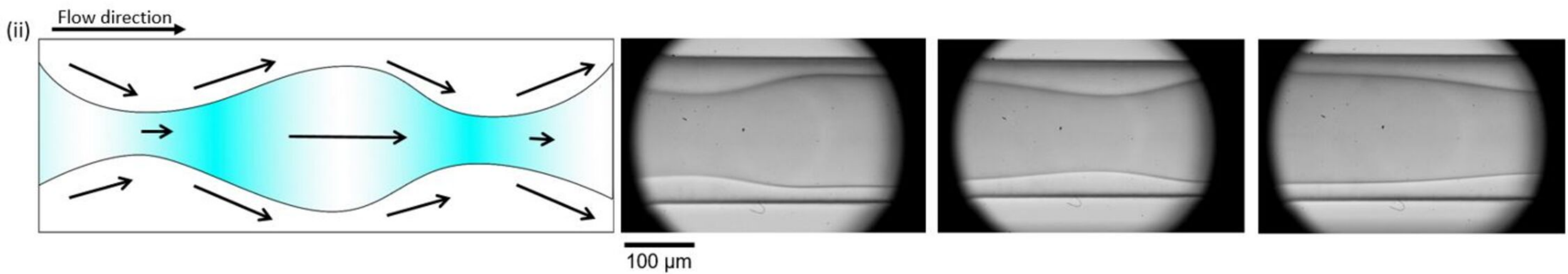
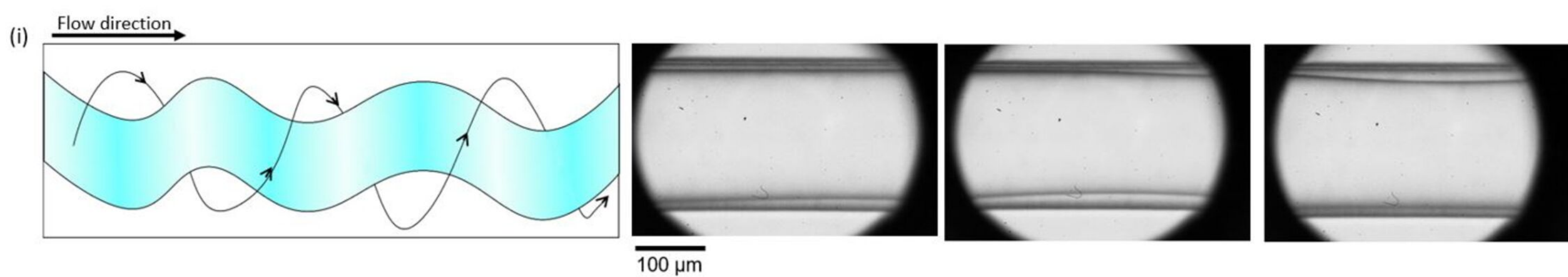
100  $\mu\text{m}$

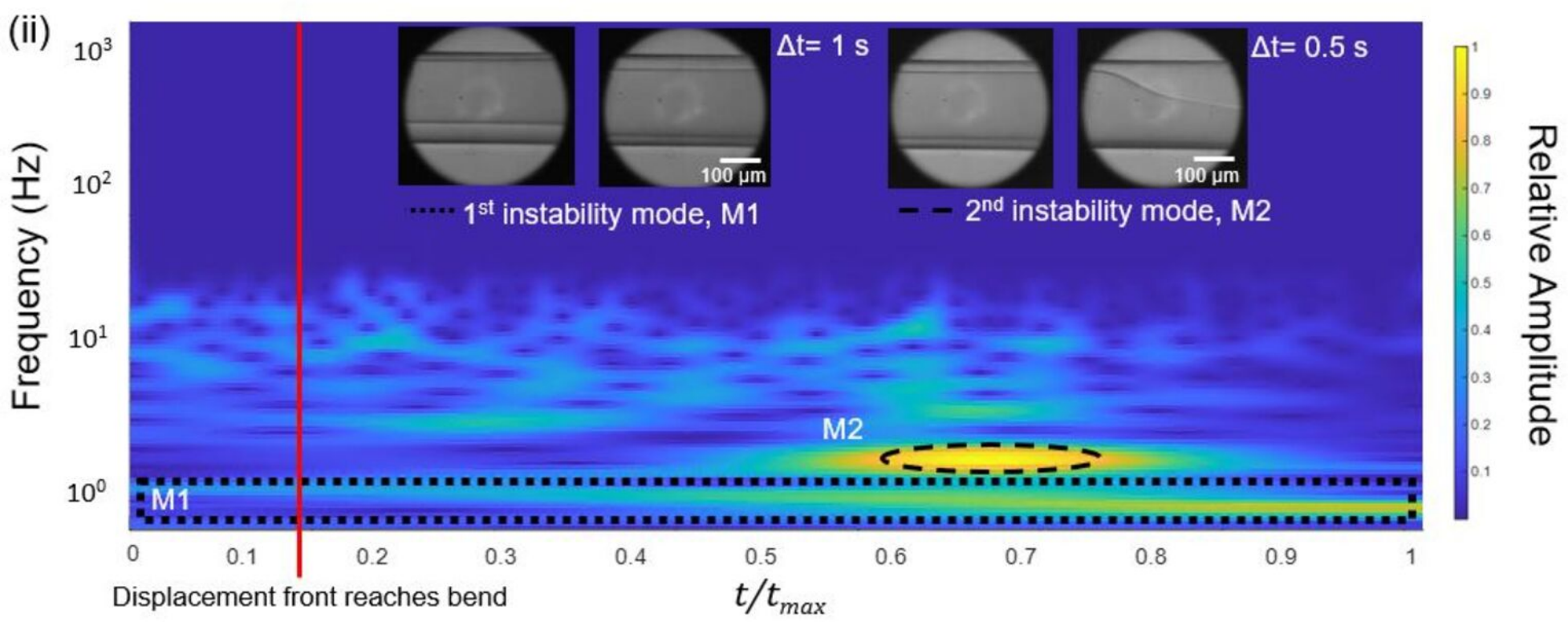
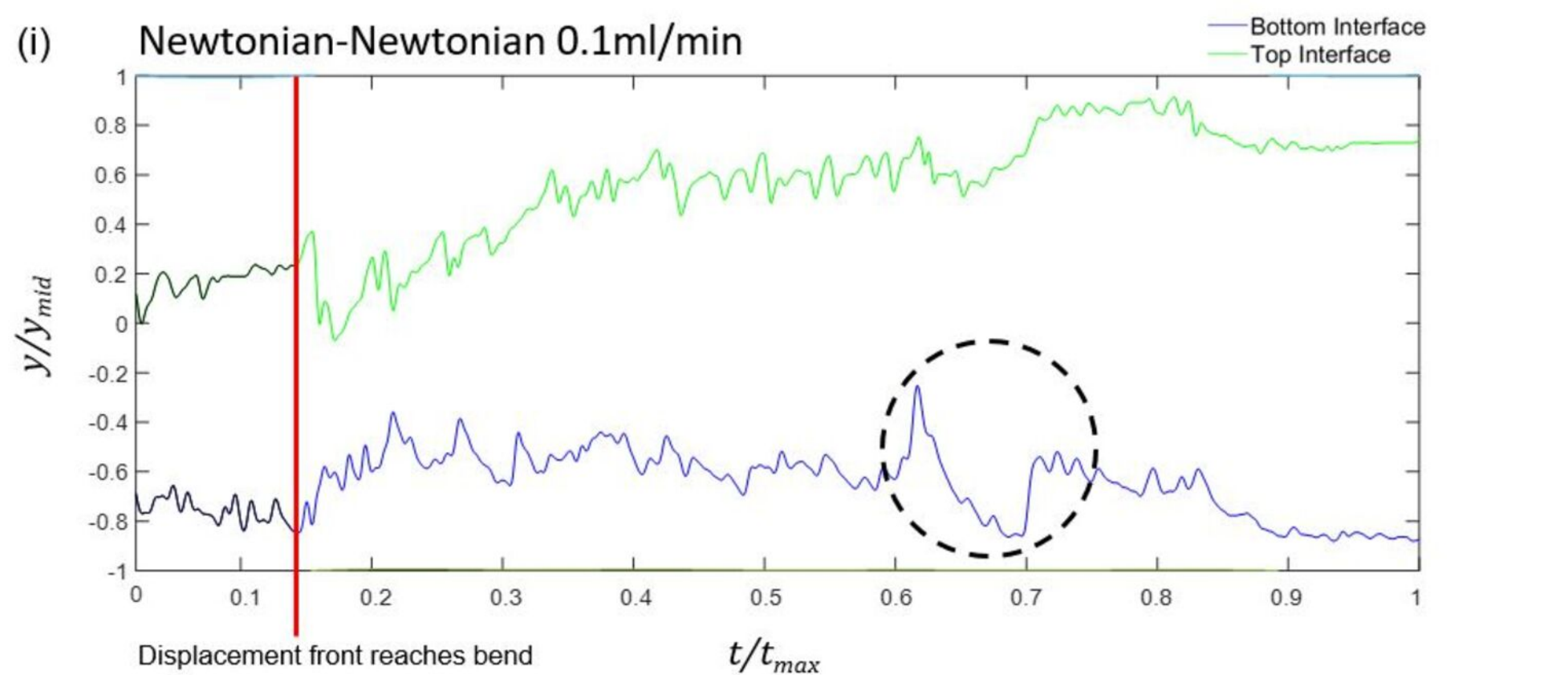
Dimensionless Film Thickness,  $h/r$





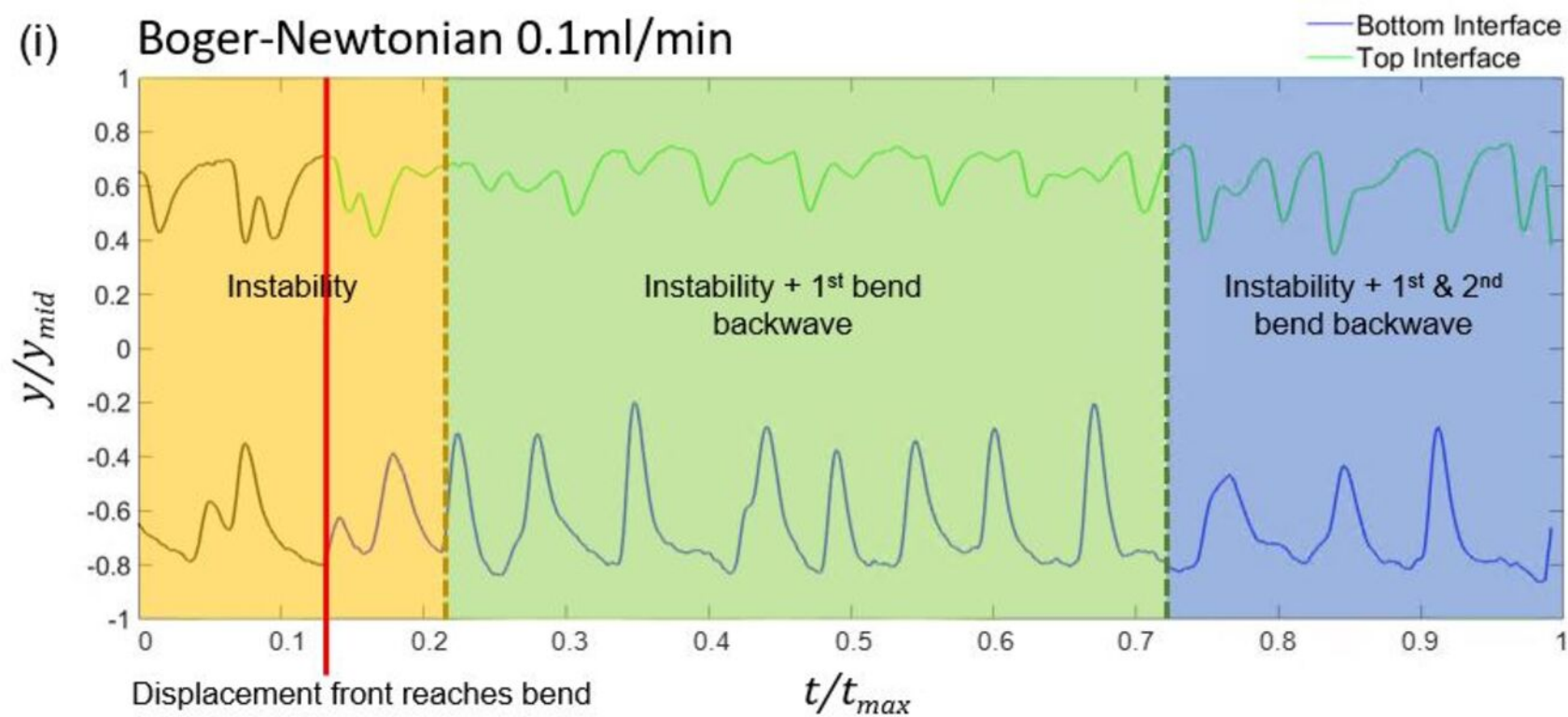




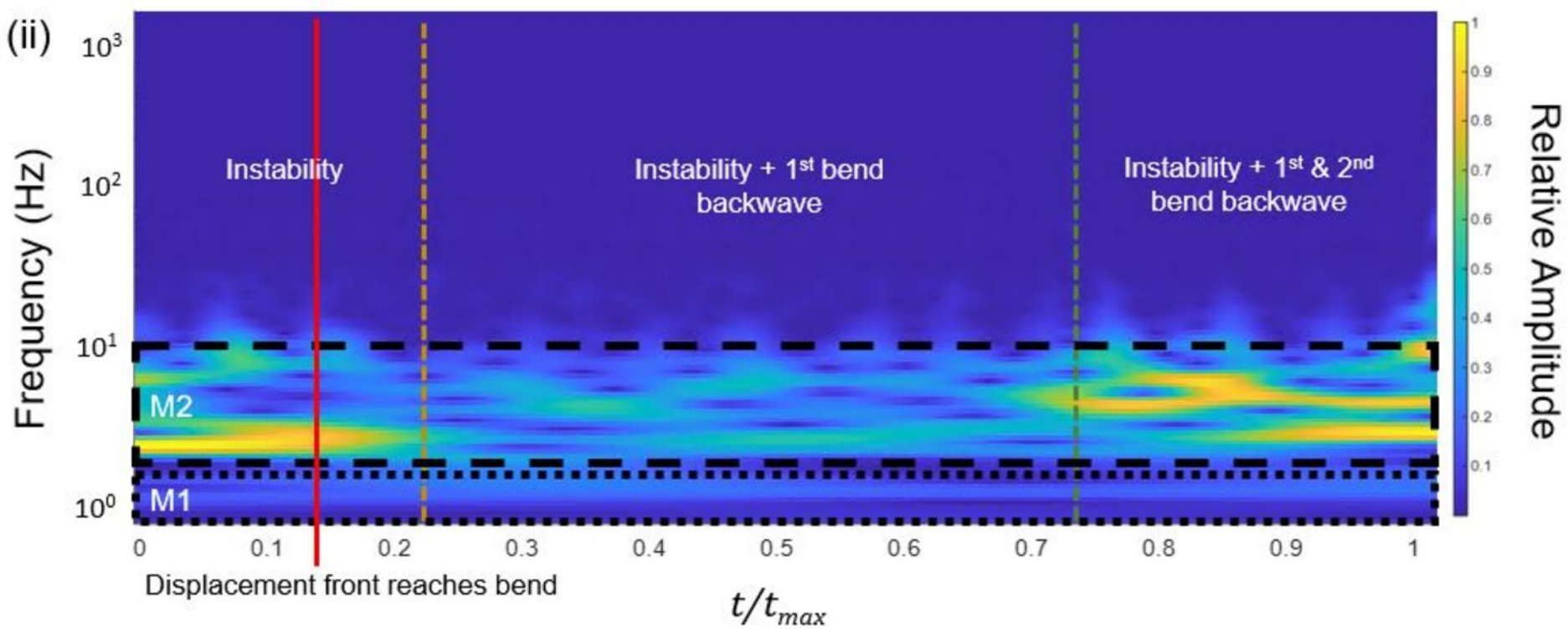




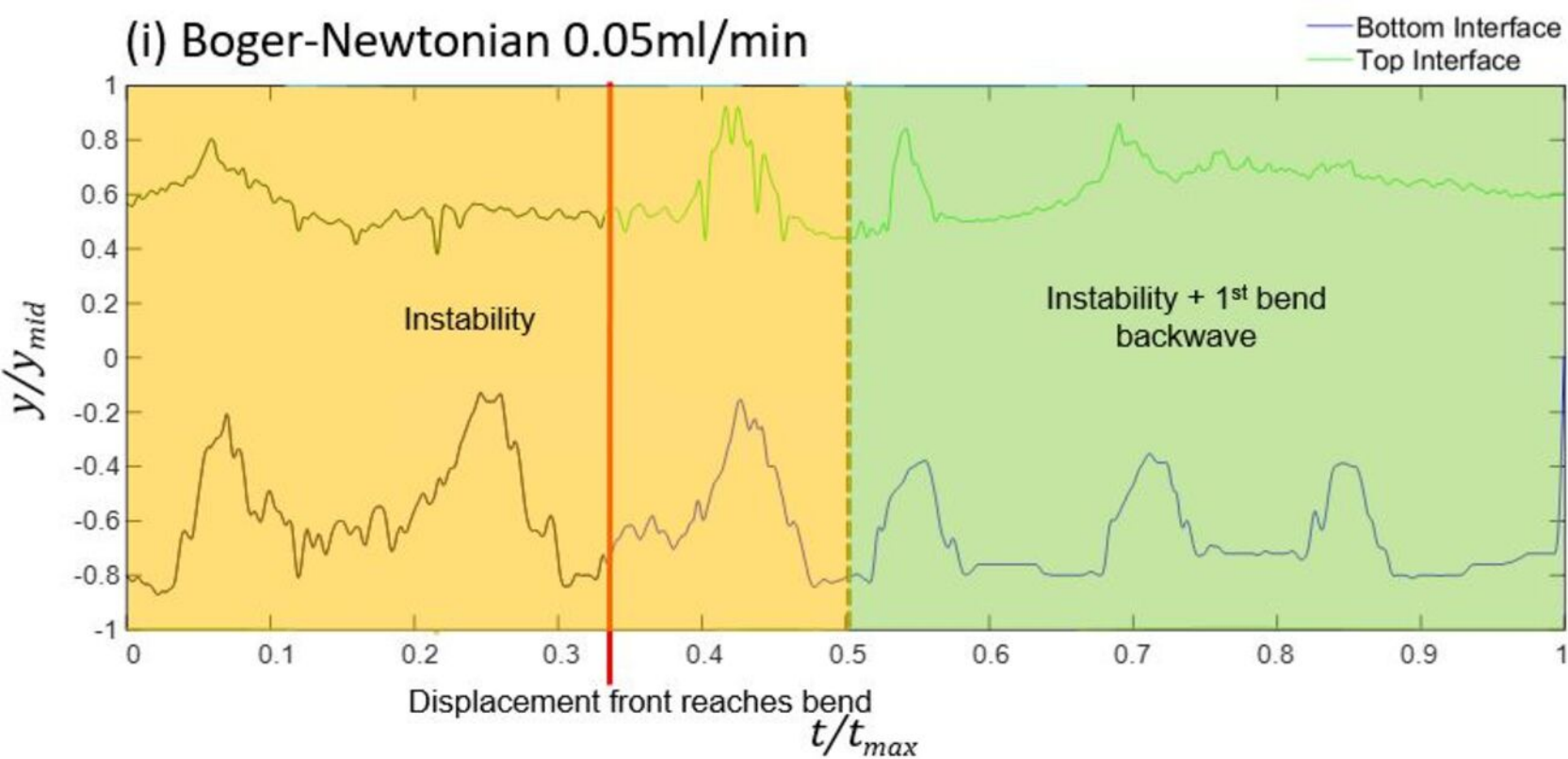
(i) Boger-Newtonian 0.1ml/min



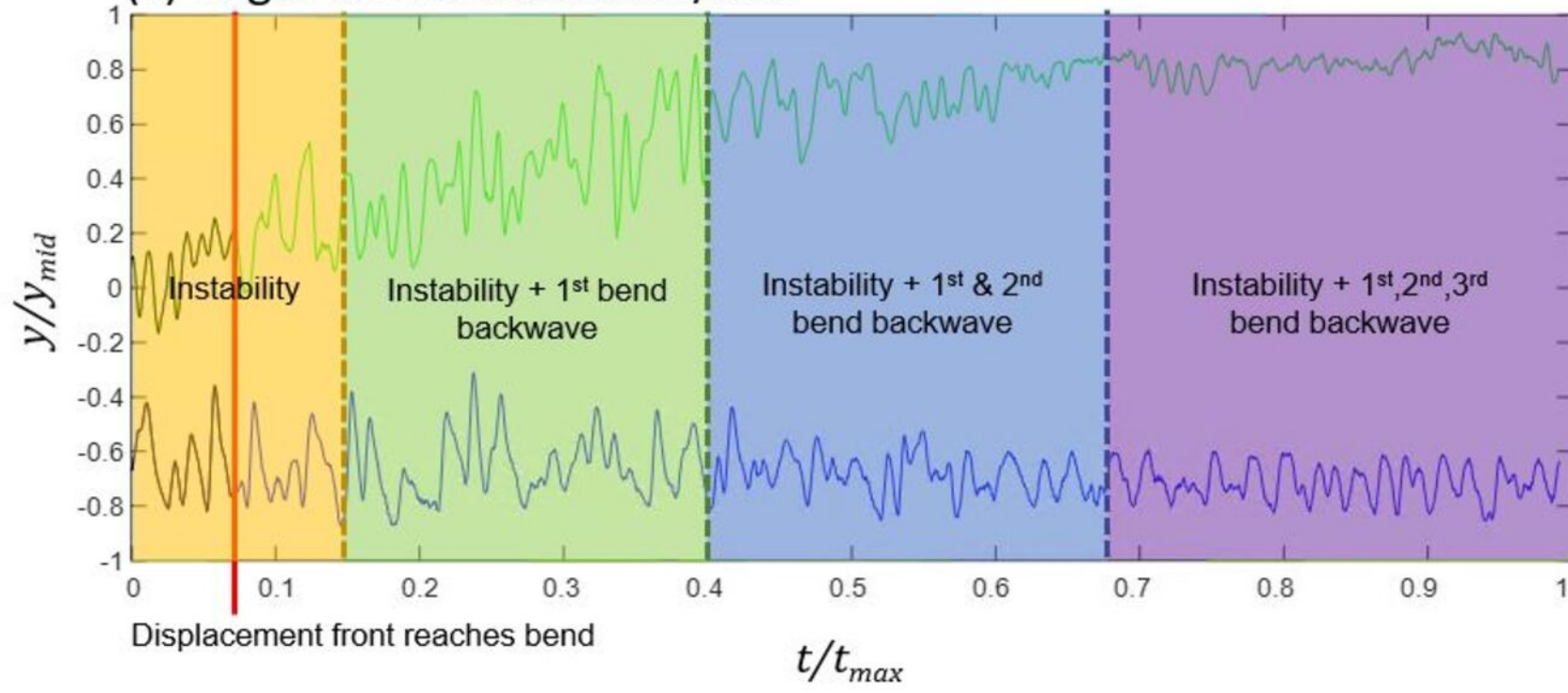
(ii)



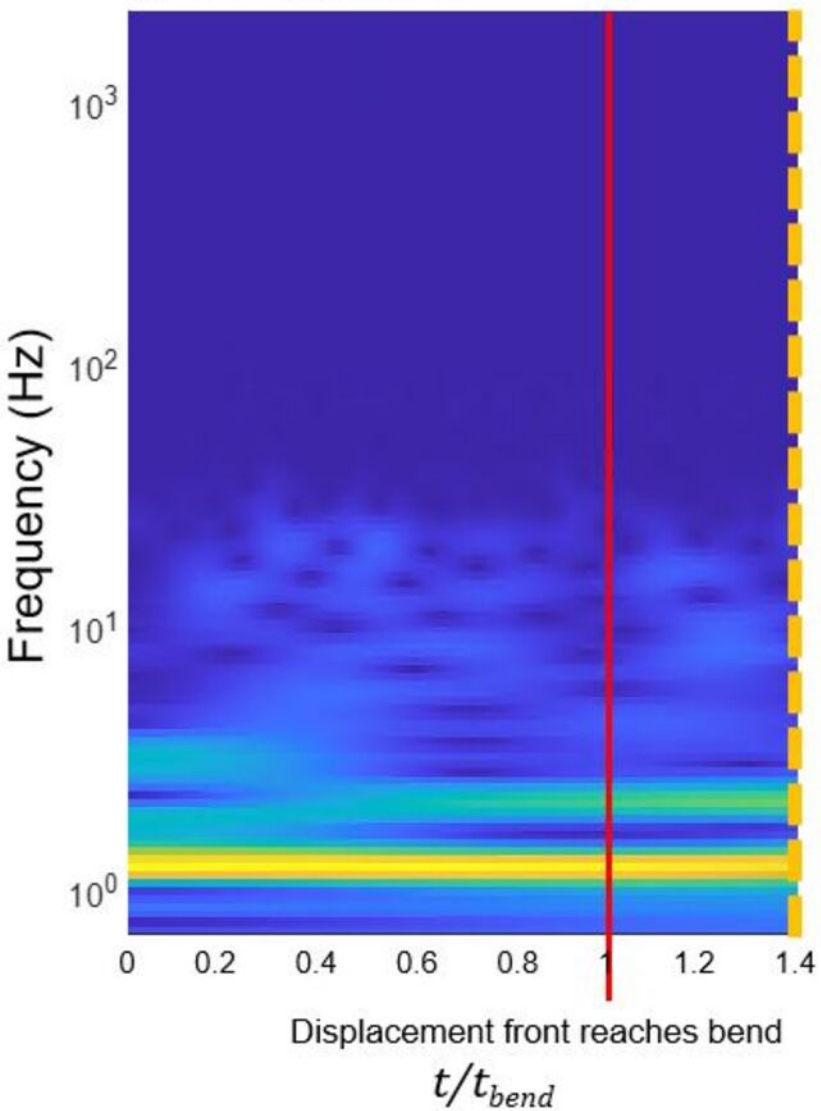
(i) Boger-Newtonian 0.05ml/min



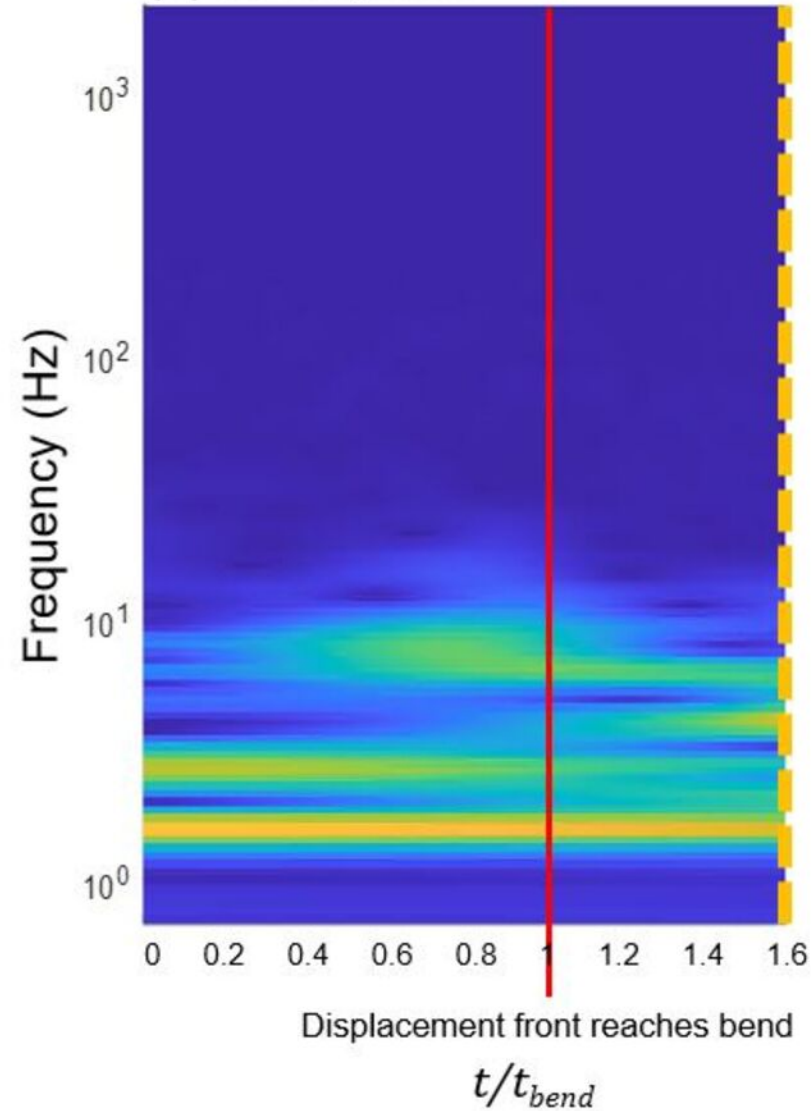
(ii) Boger-Newtonian 0.2ml/min



(i) 0.05 ml/min



(ii) 0.1 ml/min



(iii) 0.2 ml/min

